1996

Hydrodynamics of sediment suspensions in the littoral zone of the lower York River - Phase II

John D. Boon
Virginia Institute of Marine Science

Hydrodynamics of Sediment Suspensions in the Littoral Zone of the Lower York River - Phase II

by

John D. Boon

Virginia Institute of Marine Science and
School of Marine Science, College of William and Mary
Gloucester Point, Virginia 23062

December 1996

This study was funded, in part, by the Virginia Coastal Resources Management Program at the Department of Environmental Quality through **Grant No. NA57OZ0561-01** of the **National Oceanic and Atmospheric Administration**, Office of Ocean and Coastal Resources Management, under the CZM Act of 1972, as amended.

Hydrodynamics of Sediment Suspensions in the Littoral Zone of the Lower York River - Phase II

by

John D. Boon

Virginia Institute of Marine Science and
School of Marine Science, College of William and Mary
Gloucester Point, Virginia 23062

December 1996

This study was funded, in part, by the Virginia Coastal Resources Management Program at the Department of Environmental Quality through **Grant No. NA57OZ0561-01** of the **National Oceanic and Atmospheric Administration**, Office of Ocean and Coastal Resources Management, under the CZM Act of 1972, as amended.

CONTENTS

List of Figures

I. Introduction

This report covers the second year (Phase II) of a two-year study. An earlier contract report (Boon, 1996) was submitted in January, 1996, to the Virginia Coastal Resources Management Program covering the first year (Phase I) results of a wave, current and suspended sediment monitoring study conducted at the mouth of the York River (Figure 1).

The purpose of the monitoring study, as originally planned, was to investigate processes governing sediment suspension within the shallow waters of the littoral zone (depths < 2m) in coastal estuaries. These are regions in which bottom sediment, in the absence of vegetative cover and depending on sediment grain sizes present, has the potential to be actively eroded and entrained in the water column by wind waves and/or currents. Suspended sediment has the further potential to impact water quality and promote eutrophication through nutrient enrichment processes (Kemp et al., 1983; Orth and Moore, 1983). High sediment loadings also lead to light reduction in the photic zone which can impact the growth or survival of submerged aquatic vegetation (De Groot and de Jonge, 1990).

The modeling of suspended sediment distributions in shallow water involves two principal tasks: 1) describing the processes by which sediment is entrained and/or deposited at the sea bed and 2) describing the processes governing its spatial and temporal distribution within the water column. Local entrainment or deposition refers to sediment added or subtracted from the base of the water column locally and is commonly related to the properties of the bed (sediment grain size, bed roughness) and the fluid shear stresses acting on the bed. Bed shear stresses result from combined wave and current action near the bed and usually involve processes that are unsteady. For this reason, time series (simultaneous observations) of sediment concentration and fluid velocity are useful when measured at time scales appropriate to wave and current motion. However, local changes in concentration may occur that have nothing to do with local changes in velocity or shear stress. Advective change can occur wherever spatial gradients in sediment concentration are found in the presence of a steady current. Spatial gradients in water depth and bottom sediment type are especially pronounced at littoral zone boundaries and tend to promote strong gradients in suspended sediment concentration in energetic environments regardless of whether the forcing is wind, tidal or density-driven.

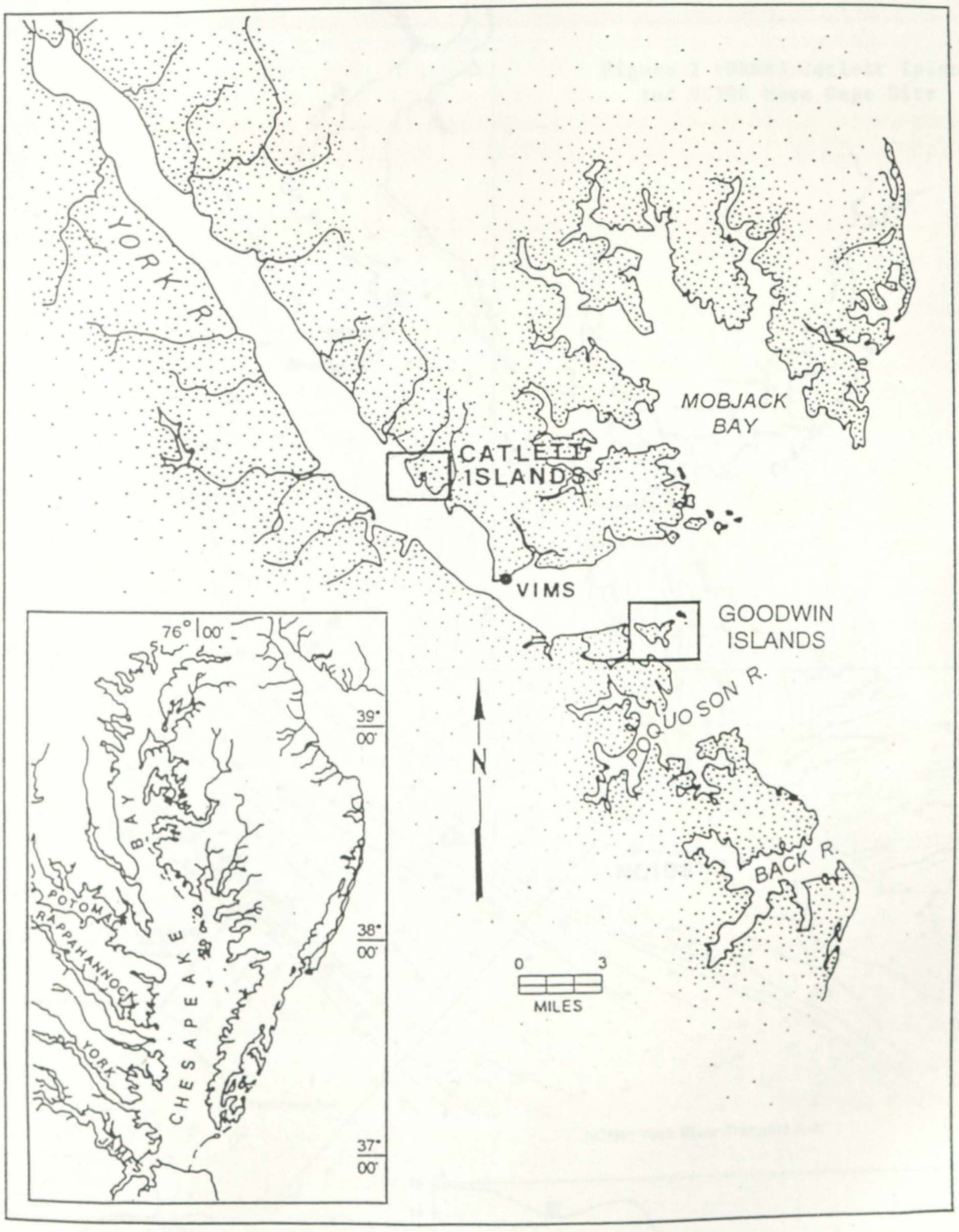

Figure 1. Location of NERRS study sites on the York River.

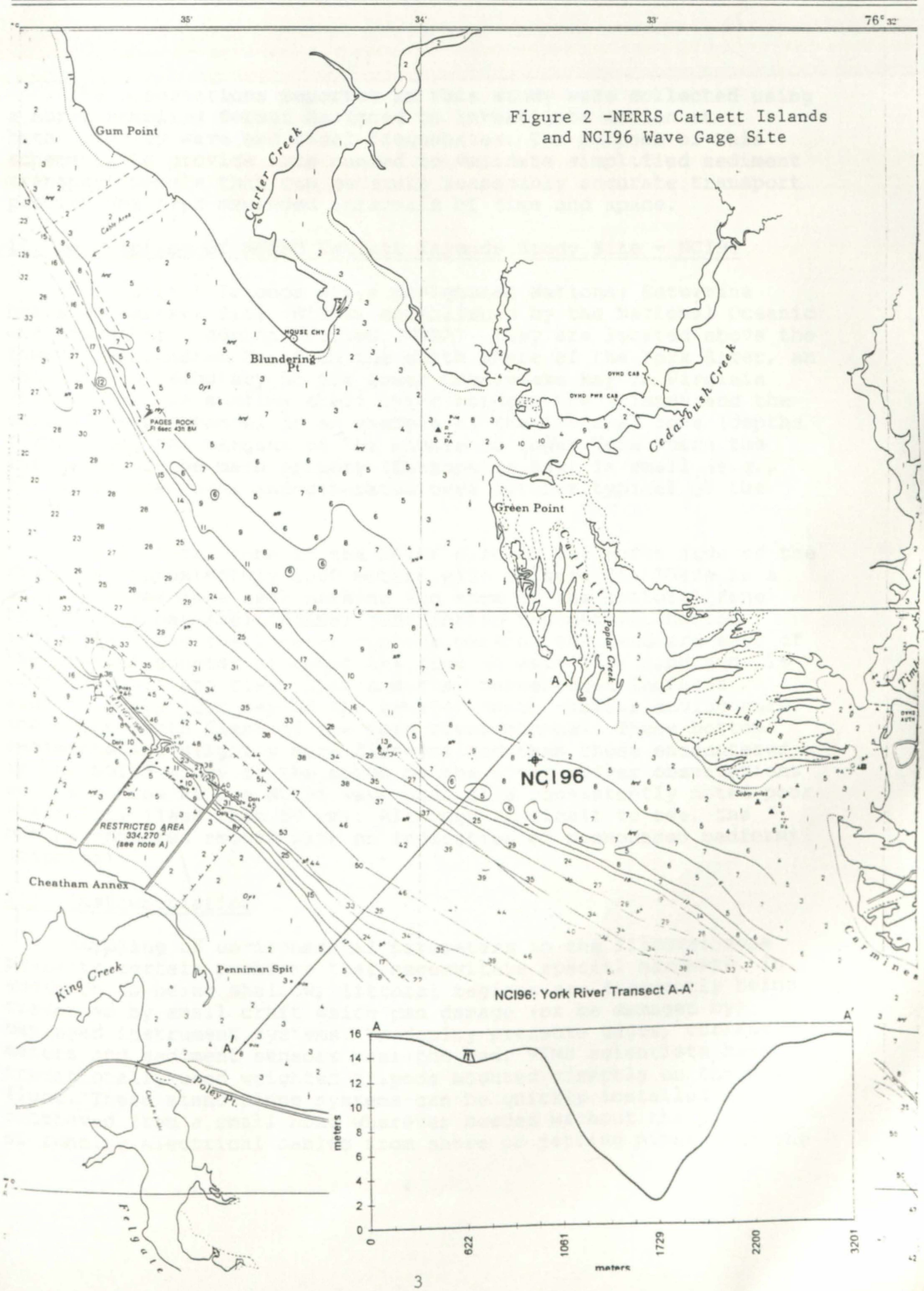

Figure 2 -NERRS Catlett Islands and NCI96 Wave Gage Site

The observations reported in this study were collected using a burst-sampling format designed to investigate motion at both gravity wave and tidal frequencies. The purpose of this scheme is to provide data needed to validate simplified sediment transport models that can generate reasonably accurate transport predictions over expanded intervals of time and space.

II. Description of NERRS Catlett Islands Study Site - NCI96

The Catlett Islands are a designated National Estuarine Research Reserve Site (NERRS) established by the National Oceanic and Atmospheric Administration (NOAA). They are located above the town of Gloucester Point on the north shore of the York River, an estuary and tributary to the lower Chesapeake Bay in Virginia (Figure 2). The shallow shelf lying between the islands and the central river channel is an example of the littoral zone (depths < 2m) along the margins of the middle to lower York where the influence of the main estuary (Chesapeake Bay) is small (e.g., all waves are local and generated over fetches typical of the river).

The littoral zone at the NCI96 site on the north side of the river is approximately 1000 meters wide (Figure 2). There is a shallow levee-like bank marking the edge of the littoral zone here with a parallel channel just inside the margin. Bottom sediments along the 2-meter contour marking the landward edge of the channel consist of about 89% fine to very fine sand and 11% combined silt and clay. Silt and clay percentages increase significantly just beyond the 2-meter depth contour moving onto the steep north flank of the main river channel. These bottom sediments are slightly more fine-grained than those encountered in the NGI95 study at the mouth of the river. Diver observations of the bottom at the NCI96 wave gage site consistently noted poor visibility (less than 50 cm). Although difficult to see, the bottom appeared smooth with no indication of pronounced bedforms (ripples).

III. Instrumentation

Sampling of environmental parameters in the littoral zone presents certain problems that necessitate special hardware. In addition to being shallow, littoral regions are frequently being traversed by small craft which can damage (or be damaged by) deployed instrument systems. To deploy pressure gages, current meters and sediment sensors near the bed, VIMS scientists have traditionally used weighted tripods mounted directly on the bay floor. These stand-alone systems can be quickly installed and retrieved from a small boat wherever needed without the problem of running electrical cables from shore or jetting pipes into the

bottom. A special low-profile tripod was used at NGI95 (Figure 3) which did not protrude above the free surface and was marked by a series of high-visibility PVC traffic poles positioned around it.

In spite of the clear markings surrounding our wave gage, or perhaps because of them, on May 27 parties unknown saw fit to remove all of our equipment and place it on the adjacent beach! Equipment damage was minor and no data were lost. However, given the apparent risk and the near-completion of the planned series of observations at this site, re-deployment of the gage was not attempted.

III.a P4 Shallow-Water Wave Gage - In its basic configuration, the low-profile tripod was equipped as a low-maintenance wave gage (wave height, period and direction) designed to operate over a time span of several months. To form a shallow-water, directional wave gage, four Sensotec Model Z pressure sensors (0-15 psig) were mounted on the tripod in the configuration shown in figure 3. An on-board magnetic compass provided information on array orientation and a Tattletale Model T6 microcomputer made by Onset, Inc. controlled data acquisition. Power for the T6 and the pressure sensors was delivered via a heavy, strain-bearing conductor cable running from the tripod to a small weighted pallet containing the main battery housing. To replace batteries (required every two weeks) the pallet and cable were raised from the bottom and used as a mooring for a small boat sent to retrieve and service the housing. The mooring/conductor cable also provided a communications pathway for uploading stored data from the T6 hard drive to a portable PC operated by personnel aboard the boat. Between servicing visits, the T6 computer was programmed to sample pressure (P4) data every hour on the hour using a one-hour burst interval, a sampling rate of 2 Hz and a sample size of 512 readings for each sensor.

Following data retrieval, calibration parameters supplied by Sensotec with each pressure sensor were used to convert raw datato engineering units. These pressure readings were in turn converted to fluctuating sea surface elevations using the hydrostatic equation and linear wave theory to correct for frequency-dependent amplitude attenuation (minor at the depths involved). Dynamic tests were conducted in the VIMS laboratory flume to verify adequate sensor response to periodic motion at frequencies up to 0.5 Hz.

Using the corrected P4 data series, directional wave spectra were computed using the parametric method of Longuet-Higgins, Cartwright and Smith (1963) as applied to a 'star' array (Goda, 1985). Standard wave parameters (IAHR, 1989) including zero-moment wave height (Hm_o) and zero-upcrossing period (T_z) were

computed from the individual pressure series. Near-bottom orbital velocity amplitude, U_b, was calculated using

$$U_b = \frac{\pi H m_0}{T_z \sinh(kh)}$$

where $k = 2\pi/L$ is the wave number, L = wavelength, h = water depth. Given wave period and water depth, k and the factor kh were determined from the dispersion equation

$$\omega^2 = gk \tanh(kh)$$

in which $\omega = 2\pi/T_z$ is the wave radian frequency corresponding to T_z.

III.b PUV Wave and Current Gage - A Sea Data Model 635-9RS wave and current meter was mounted on the tripod and operated for a four-week period. The tripod had to be raised to deploy and retrieve this instrument which received power from a secondary battery housing mounted horizontally along the bottom of the tripod frame. Pressure (P) and horizontal velocity (U,V) components were sensed by a Paroscientific digiquartz pressure sensor and Marsh-McBirney 2-axis remote electromagnetic current probe with 4 cm spherical sensor, respectively. A separate Tattletale Model T6 microcomputer and power supply were mounted adjacent to one another in the 635-9RS unit. The pressure sensor was mounted at a height of 20 cm and the velocity sensor at a height of 100 cm above the bed.

The logger was set to record its first burst at 1200 EST on 25 April, 1996; Thereafter, burst samples of PUV data (1024 samples per burst) were collected every three hours at a sampling rate of 2 Hz.

Pressure readings from the Paroscientific sensor were converted to fluctuating sea surface elevations using similar procedures to those described for the Sensotec gages. Velocity readings from the Marsh-McBirney electromagnetic current meter were corrected and verified using pre- and post-experiment calibrations performed in a 20 m recirculating flume at VIMS.

Directional wave spectra can be calculated with PUV data using essentially the same program described for the P4 'star' array. To avoid rendundancy, this was not done. Instead, a calculation of what is termed the Principal Wave Direction (PW_DIR) was made using the U,V velocity data in each burst; i.e., by axis rotation, the principal axis or component U' was

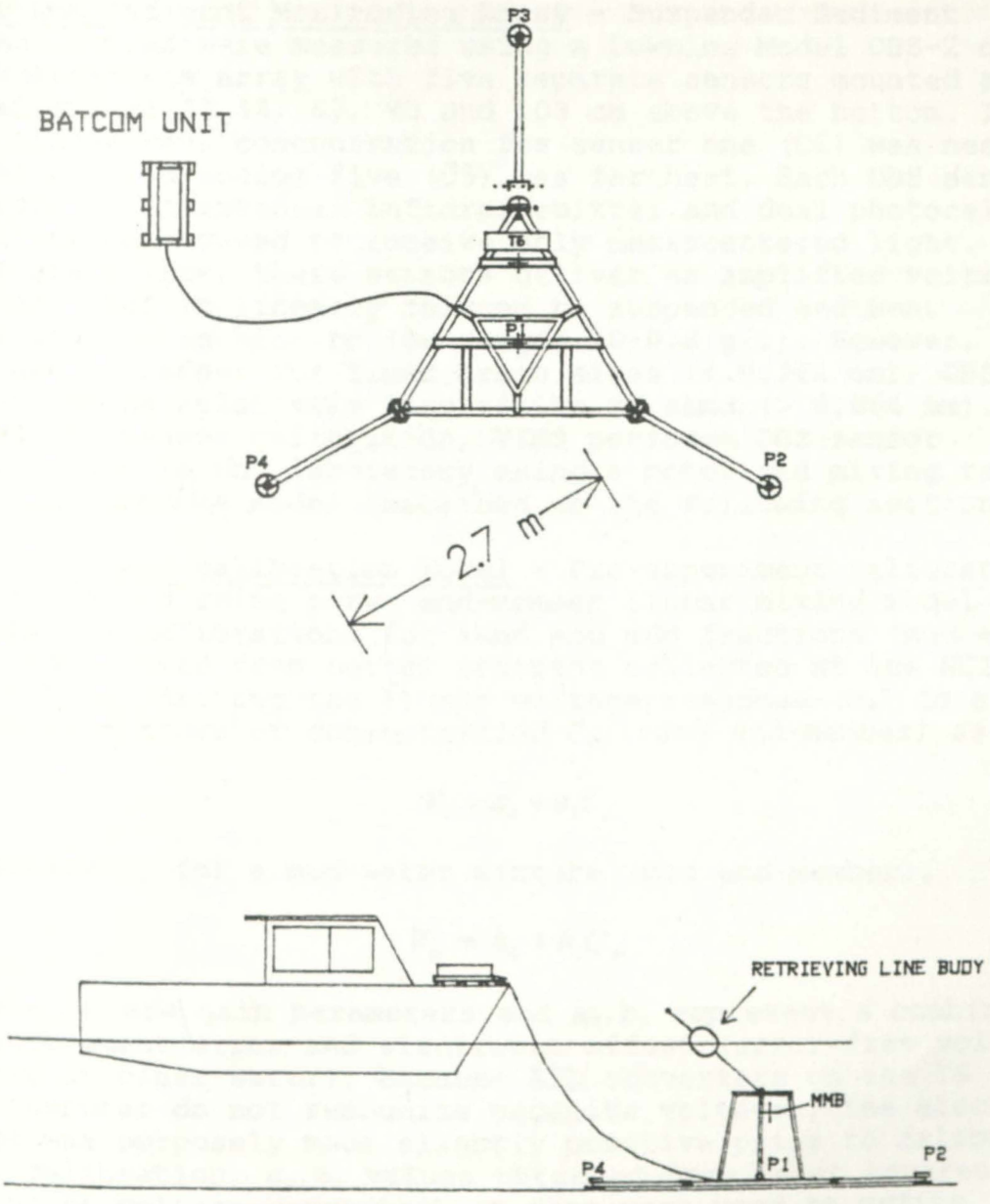

Figure 3. Shallow Water Wave Gage

found which contained the maximum variance. The 180° ambiguity in wave direction was resolved by correlating U' with the pressure signal assuming a linear, progressive wave train.

III.c OBS Sediment Monitoring Array - Suspended Sediment concentrations were measured using a Downing Model OBS-2 optical backscatterance array with five separate sensors mounted at elevations of 23,43, 63, 83 and 103 cm above the bottom. In the resulting array, concentration for sensor one (C1) was nearest the bottom and sensor five (C5) was farthest. Each OBS sensor consists of an integral infrared emitter and dual photocell with IR filter configured to receive only backscattered light. For a given grain size, these sensors deliver an amplified voltage response that is linearly related to suspended sediment concentration in mid- to low-ranges (0-0.8 g/l). However, the response is larger for finer grain sizes (< 0.064 mm), OBS sensors being relatively insensitive to sand (> 0.064 mm). To obtain the proper calibration, VIMS performs OBS sensor calibrations in the laboratory using a motorized mixing tank and a linear response model described in the following section.

III.c.1 Linear calibration model - Pre-experiment calibrations were performed using a two end-member linear mixing model based on separate calibrations for sand and mud fractions (mud = silt + clay) wet-sieved from bottom sediment collected at the NCI96 tripod site. Writing the linear voltage response (V_s) to a sand and water mixture of concentration C_s (sand end-member) as

$$V_s = a_0 + a_1 C_s$$

and similarly for a mud-water mixture (mud end-member),

$$V_m = b_0 + b_1 C_m$$

where a_1, b_1 are gain parameters and a_o, b_o represent a combination of measurement error and electronic offset (error-free voltage reading in clear water). Because ATD converters on the T6 microcomputer do not recognize negative voltages, the electronic offset was purposely made slightly positive prior to calibration. After calibration, a_o, b_o values obtained from least squares fitting of voltage-concentration data were used to define corrected voltages; i.e., $V_s' = V_s - a_o$ and $V_m' = V_m - b_o$.

The linear mixing model (Green and Boon, 1992) assumes that a total voltage equal to the sum of the corrected partial voltages will be sensed in the field environment where both end-members are present in fixed (known) proportions and occupy the same fluid volume. In the latter circumstance, each concentration (sand or mud) can be represented as a fraction of the total concentration, C_t,

$$C_s = f_s C_t$$
$$C_m = f_m C_t$$

where the fractions of sand (f_s) and mud (f_m) refer to the fractional amount (dry weight) of the total material suspended within the sample volume; i.e., $f_s + f_m = 1$. The total voltage is then represented by

$$V_t = \bar{a}_0 + V_s' + V_m' = \bar{a}_0 + (a_1 f_s + b_1 f_m) C_t$$

and the total concentration is found using

$$C_t = \frac{V_t - \bar{a}_0}{a_1 f_s + b_1 f_m}$$

where $\bar{a}_0$ is the average offset of the OBS sensor.

A two end-member linear mixing model can also be used (with caution) when the voltage response for one of the end-members is non-linear. This is usually the case when the 'mud' end-member has a low silt to clay ratio; a better empirical fit is then obtained using

$$V_m = b_0 + b_1 C_m + b_2 C_m^{\,2}$$

Introduction of the latter equation in place of the linear expression for mud yields a quadratic solution for C_t. Quadratic solutions for OBS sediment data yield a singular concentration associated with a voltage maximum; lesser voltages are ambiguous; i.e., they can be produced by either a high range or a low-range concentration. Direct analysis of supplemental water samples is then required if high range concentrations are deemed likely to occur in the field environment under investigation. The ambiguity problem is most severe near the voltage maximum where the (sensor) sensitivity to concentration change reaches a minimum.

The two end-member OBS calibration model used in the present NCI96 study is illustrated by the graphs included in

Appendix A. Based on sediment grain size data obtained from a sediment trap, the representative fractions f_s and f_m form the ratio $f_s:f_m = 6:94$. This implies that the mud end-member is highly dominant and that the singular concentration is closely approximated by $C_m = -b_1/2b_2$ or about 1 g/l.

IV. Wave, Wind and Current Observations

The following sections present descriptions of the wave and current parameters measured at the NCI96 site. These measurements were made during the period February 15 to May 27, 1996. The shallow-water gage was removed on April 23 for cleaning and repair. It was re-deployed at the NCI96 site on April 25, 1996.

IV.a Wave parameters - Basic wave parameters (Hm_o, T_z and U_b) were determined for each burst made with the shallow-water wave gage pressure (P4) array from February 15 until May 27, 1996. These parameters are shown in figures 4 through 11.

Wave activity in February, March, April and May 1996 was generally low at the NCI96 site. Relatively few storms or frontal systems occurred that produced Hm_o wave heights in excess of 0.10 m. Interestingly, two 'events' occurred in March and April that very briefly produced Hm_o wave heights of approximately 0.50 m. As shown in figures 12 and 13, the wave trains observed during these events displayed considerable 'groupiness' with the highest individual waves in the largest groups approaching 0.8 m in height measured trough to crest. These freakish waves were of short duration; i.e., longer than the 8.5-minute burst duration of the P4 sampling array but less than the one-hour interval between bursts.

Wave periods, T_z, were always on the order of 2 to 3 seconds during wave events ($Hm_o > 0.10$ m). Some long period (6 to 8 second) swell were observed but always of a very low height (1 to 4 cm). Wave orbital velocities, U_b, were low, not exceeding 0.10 m/sec except briefly during the two to three wave 'events' that occurred each month. This strongly suggests that waves acting alone are capable of mobilizing very little sediment at the bed.

IV.b Wind speed and direction - Wind speed and direction are routinely monitored at the VIMS campus in Gloucester Point (Figure 1) where the speed and direction sensor is mounted on a tower approximately 18 m above sea level. Wind vectors (stick diagrams) for February, March, April, and May, 1996 are shown in Figures 14 through 17. As expected, higher waves are associated with strong winds from the west to west-northwest directions.

IV.c Directional wave spectra - Directional wave spectra are a particularly useful tool for studies of the wave climatology of a region. By portraying the distribution of wave energy density as a function of frequency and direction, one can determine how wave trains develop during the various stages of a storm, determine if multiple frequencies and directions are involved and get a feel for the directional spreading associated with a given peak frequency.

An example of selected directional wave spectra are presented as 3-D mesh plots in figures 18 and 19. In these figures, wave direction (measured 0° - 360° clockwise from true north) is the direction toward which the waves are moving, not the direction they are coming from. A code is shown in the upper right corner of each figure identifying the year, month, day and hour of the burst of data yielding the spectrum; e.g., the code Y9630804 refers to year 96, month 3, day 8 and hour 4 (0400 EST).

The dominant spectral peak appearing in figures 18 and 19 represents a wave train heading east (90) with a frequency of 0.4 Hz. As the wind waves attain their highest energy, other spectral peaks appear at the same frequency (0.4 Hz) but indicate other directions. It is uncertain whether the directional information in these secondary peaks is meaningful or not because of limitations inherent in the array size and the method of analysis used (Longuet-Higgins, Cartwright and Smith, 1963). What is certain, however, is the fact that strong groupiness is present in the highest wave fields observed at the NCI96 site (e.g., Figure 12); groupiness occurs when multiple wave trains of similar amplitude but slightly different frequency are present in a sea. At such times there should be a departure from a single narrow peak in the resulting directional wave spectrum.

IV.d Wave and current - Measurements taken with the Sea Data 635-9RS wave and current meter provide a 'PUV' time series consisting of pressure4(P) combined with 2-axis, horizontal (U,V) velocity components. Although directional wave spectra can also be computed using PUV data, this would be rendundant since we already obtain that information from the longer running P4 data series. Determination of the Principal Wave Direction (see p.10) provides a useful burst-summary parameter similar to the zero-upcrossing wave period, Tz, for use in a data base compilation. However, similar information is also available from the P4 series analysis and, as noted above, Hm_0 wave heights have been minimal to the point that directional information offers little practical benefit.

Current information from the 2-axis Marsh-McBirney current meter (sensor located 1.0 m above the bed) was obtained from 1200

EST, April 25 until 1500 EST, May 27, through burst-sampling conducted at three-hour intervals. The mean current, absent of the wave-orbital flow but inclusive of the tidally-induced current, was approximated by the burst-mean current (U,V flow vector-averaged over the 8.5-minute duration of each burst).

One means of displaying the burst-mean current is to assign values of current speed to a set of directional class intervals (36 bins each 10^0 wide for example) and calculate the average of the current speeds that fall within each interval or find the maximum value in each interval. We did both and the results for the April-May time period are shown in figure 20. Figure 20 shows that:

1) highest burst-mean current speeds of 25 cm/s and 21 cm/s occur at 290^0 (flood) and 120^0 (ebb), respectively,
2) highest burst-maximum current speeds of 50 cm/s and 34 cm/s occur at 290^0 (flood) and 120^0 (ebb), respectively,
3) the directional spread of either current measure is fairly narrow and flood currents are dominant compared to ebb currents.

Although waves are often responsible for the entrainment of bottom sediment in shallow environments, they do not appear to be capable of playing that role at the NCI96 study site. Except for very brief periods of time (minutes rather than hours), wave orbital velocities rarely exceed 10 cm/s at a 1 m height above the bed. Velocities on this order are unlikely to mobilize significant amounts of bed material. Tidally-induced currents, on the other hand, are of relatively high speed at this site and are capable of initiating bottom sediment motion for comparatively much longer periods (hours) during spring tide conditions. The TRANSPOR model of van Rijn (1993), used in Phase I of this study (NGI95), confirmed the general observation that local sediment resuspension by waves does not appear to be a dominant process at either site. The suspended sediment observations discussed in the following section are consistent with this conclusion.

V. Suspended Sediment Observations -

As in the NGI95 study, there were problems with biofouling that affected the response of the OBS sensors used to monitor suspended sediment concentration. During the April-May period at NCI96, fouling to 'saturation' eventually did occur, at least for the upper sensors (#3, #4 and #5) as shown in figure 21. Divers inspected and cleaned all five OBS sensors on May 20, 1996, at which time all five output signals returned to low levels. Two days after the May 20 visit, an electronics problem occurred which rendered the OBS record unusable thereafter.

The biofouling shown in figure 21 is not uniform from one sensor to the next nor is it steady in time. No attempt was made to correct the response of any of the sensors using a biofouling rate model. In spite of this difficulty, the early record from April 25 through May 3 remained usable and a partial response from sensor #4 may show an important relative (not absolute) change in suspended sediment concentration.

Figure 22 shows the variation in burst-mean suspended sediment concentration during the initial part of the OBS record from April 25 to May 3, 1996 before biofouling became much of a problem. In the upper panel of this figure one sees that concentration changes on the order of 20 to 40 mg/l occur regularly at intervals approximately equal to half a tidal cycle (maximum flood to maximum ebb or vice-versa) and thus are clearly tidally-driven. The only time that waves appear to have caused a similar amount of change is in burst 5 (April 26, 0000 EST) where a characteristically brief spike appears (Figure 22, upper panel). By examining burst 5 on a time scale of seconds (Figure 22, lower panel; Figure 23, both panels), one clearly sees that very small changes occur at periods characteristic of local wind waves (T_z of 2 to 3 sec); larger changes on the order of 40 mg/l occur at periods of 20-30 seconds and at even longer periods (60 seconds) toward the end of the burst (Figure 23, lower panel). Curiously, in figure 23 the longer period oscillations in concentration recorded by sensor 1 (23 cm above the bed) seem to be 180° out of phase with the oscillations occurring at sensor 5 (103 cm above the bed). Although we have no immediate explanation for this observation, it does not seem to be in any way consistent with local resuspension by wind waves.

After the event recorded in burst 5, very little change is noted on a time scale of seconds (e.g., Figure 24, burst 34). Going back to figure 21, all sensors show a general rise in sediment concentration starting just after May 3; sensor 4 in particular goes on to record a large high on May 7-8. While the absolute value of that high (in g/l) is in doubt because of biofouling, it occurs very shortly after a full moon and the peak of an unusually strong spring current accompanying an Apogean-Perigean spring tide. A maximum current of 1.7 kts (76 cm/s) was predicted in the main channel immediately adjacent to the NCI96 site at that time. Figure 25 shows May 1996 tidal current predictions for a point 1 n.mi SSE of Page Rock or about 1 km west of the NCI96 site. Sensor 4 also records another high in sediment concentration on May 18 when a new moon and another very strong spring current occurred.

Finally, evidence of very strong, tidally-driven

resuspension of bottom sediment is available through another tripod study by Kim et al., 1996, conducted in April, 1996, in the middle of the (older, 5 meter deep) secondary channel of the York approximately 10 km north of NCI96 (Figures 26 and 27). The 168-hour time series plots show a striking, phase-locked response of (bottom) suspended sediment concentration to periodic forcing by the tidal current. Maximum concentrations in this secondary channel of the York appear to reach or exceed 2 g/l coinciding with the greatest strength of current.

VI. Conclusions - The data gathered at the NERRS Catlett Islands monitoring site (NCI96) during spring, 1996, represents conditions observed along the outer margin of the littoral zone in the middle to lower York River. The data suggest that local resuspension of bottom sediment takes place at times of highest observed currents; i.e., during spring tides, especially greater than normal (Apogean-Perigean) spring tides. Waves appear to have a minor role because they very rarely (and very briefly) attain heights necessary to suspend bottom sediment. Consequently, even more so than at the NERRS Goodwin Islands site, the observed increases in near-bottom suspended sediment concentration appear to be due to the presence of high speed tidal currents.

The evidence of the present study suggests that most of the sediment loading (uptake) into the York River water column occurs at points where fine-grained bottom materials are exposed to maximum currents; i.e., currents on the order of 50 cm/s or more at a height of 1 m above the bed. This would mean that significant sediment resuspension probably occurs at the margins of the littoral zone but the primary loading occurs on the slopes and in the deeper waters of the main channel and is brought into the littoral zone through advection.

If the above hypothesis is correct, future efforts to predict suspended sediment loading in the littoral zone should be based on a combined sediment transport and current flow model as can be provided by a fine-grid hydrodynamics model of the York River and similar subestuarine systems. Attempts to predict sediment loading as a function of forecast wind waves for these systems will not only pose many difficulties, such as the proper estimation of fetch length for numerous sites and numerous wind directions, but will yield few results of practical value.

VII. References

Boon, J.D., 1996. Hydrodynamics of sediment suspensions in the littoral zone of the lower York River - Phase I. Virginia Institute of Marine Science, unpublished report.

de Groot, E.G. and V.N. de Jonge, 1990. Effects of changes in turbidity and phosphate influx on the ecosystem of the Ems estuary as obtained by a computer simulation model. *Hydrobiologia* 195: 39-47.

Goda, Y., 1985. **Random Seas and the Design of Maritime Structures**. University of Tokyo Press, 323p.

Green, M.O. and J.D. Boon, 1993. The measurement of constituent concentrations in nonhomogenous sediment suspensions using optical backscatter sensors. *Marine Geology*, 110:73-81.

IAHR, 1989. List of sea-state parameters by the International Association of Hydraulic Research (IAHR) Working Group on Wave Generation and Analysis. *J. Waterway, Port, Coastal and Ocean Engineering*, 115: 793-808.

Kemp, W.M., W.R. Boynton, J.C. Stevenson, R.R. Twilley and J.C. Means, 1983. The decline of submerged vascular plants in the upper Chesapeake Bay: summary of results concerning possible causes. *Marine Technology society Journal* 17: 78-89.

Longuet-Higgins, M.S., Cartwright, D.E. and Smith, N.D., 1963. Observations of the directional spectrum of sea waves using the motions of a floating buoy. In: **Ocean Wave Spectra**, Prentice-Hall, Englewood Cliffs, NJ, pp. 111-136.

Orth, R.J. and K.A. Moore, 1983. Chesapeake Bay: an unprecedented decline in submerged aquatic vegetation. *Science* 222:51-53.

van Rijn, L.C., 1993. **Principles of sediment transport in rivers, estuaries and coastal seas**. Aqua Publications, Amsterdam, 13 ch, 3 Appendices.

VIII. Data Figures 4 - 27

NERRS Catlett Islands Wave Site

Plot of Wave Height and Period

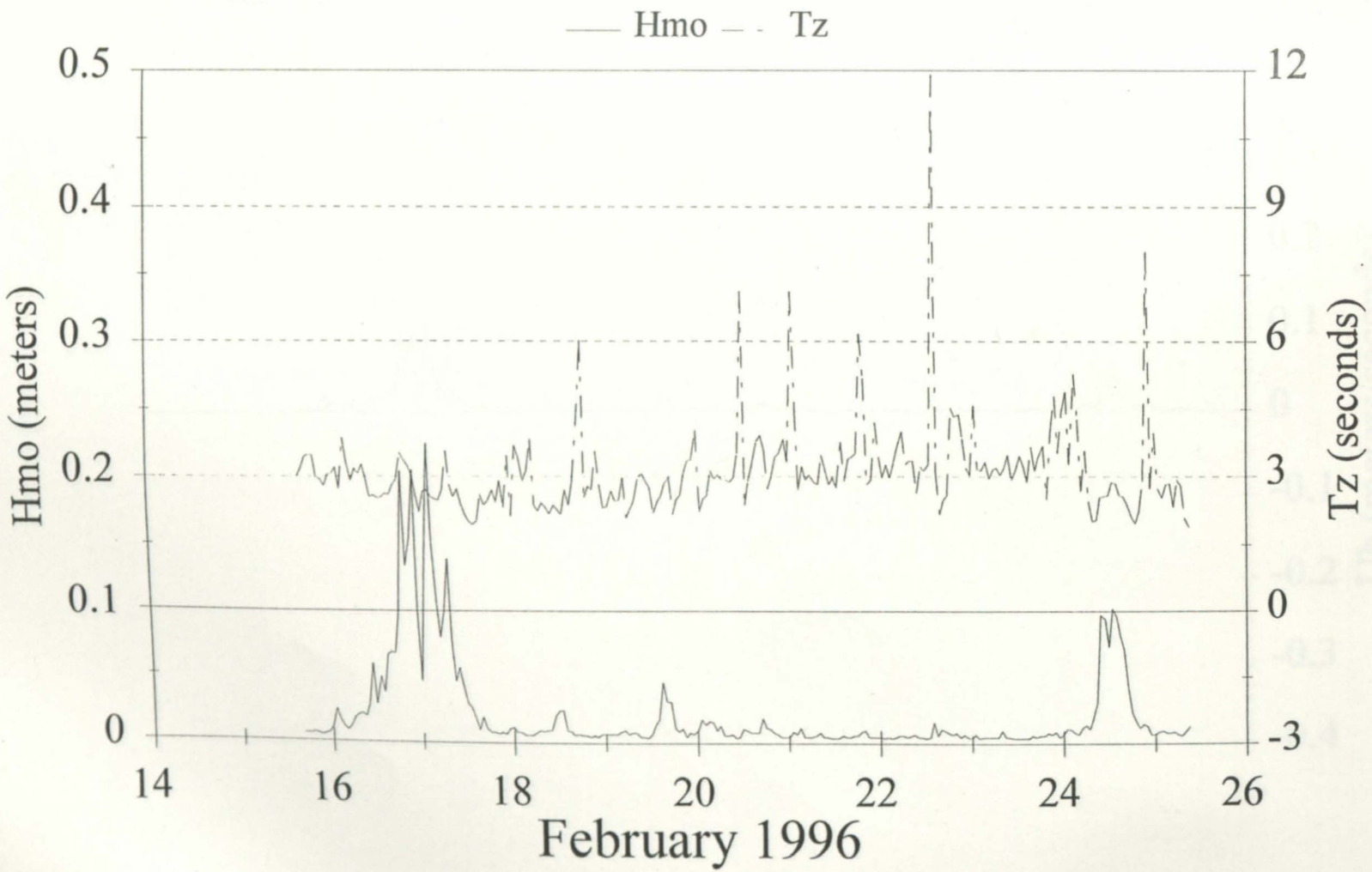

Figure 4

NERRS Catlett Islands Wave Site

Wave Height and Orbital Velocity

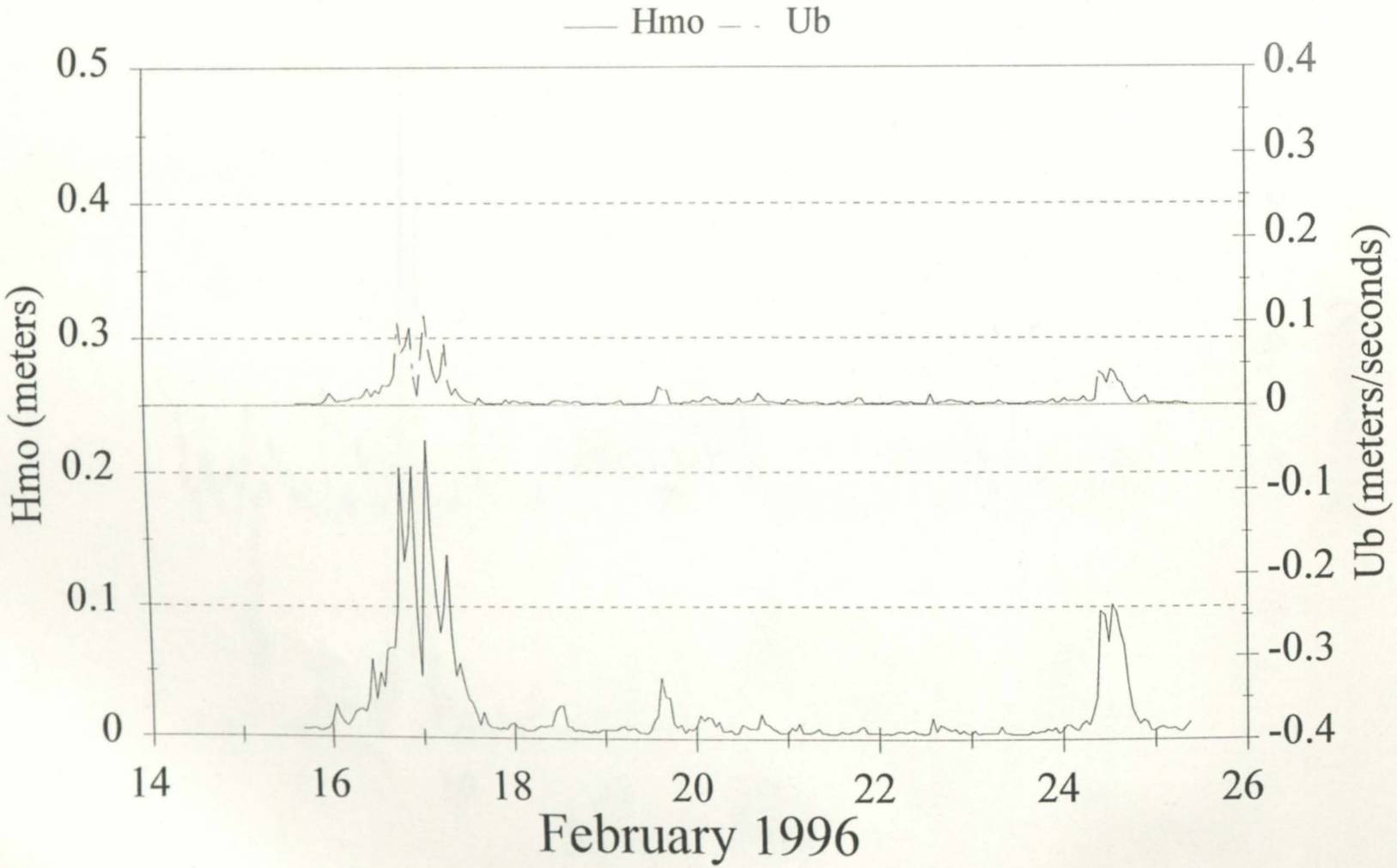

Figure 5

NERRS Catlett Islands Wave Site

Plot of Wave Height and Period

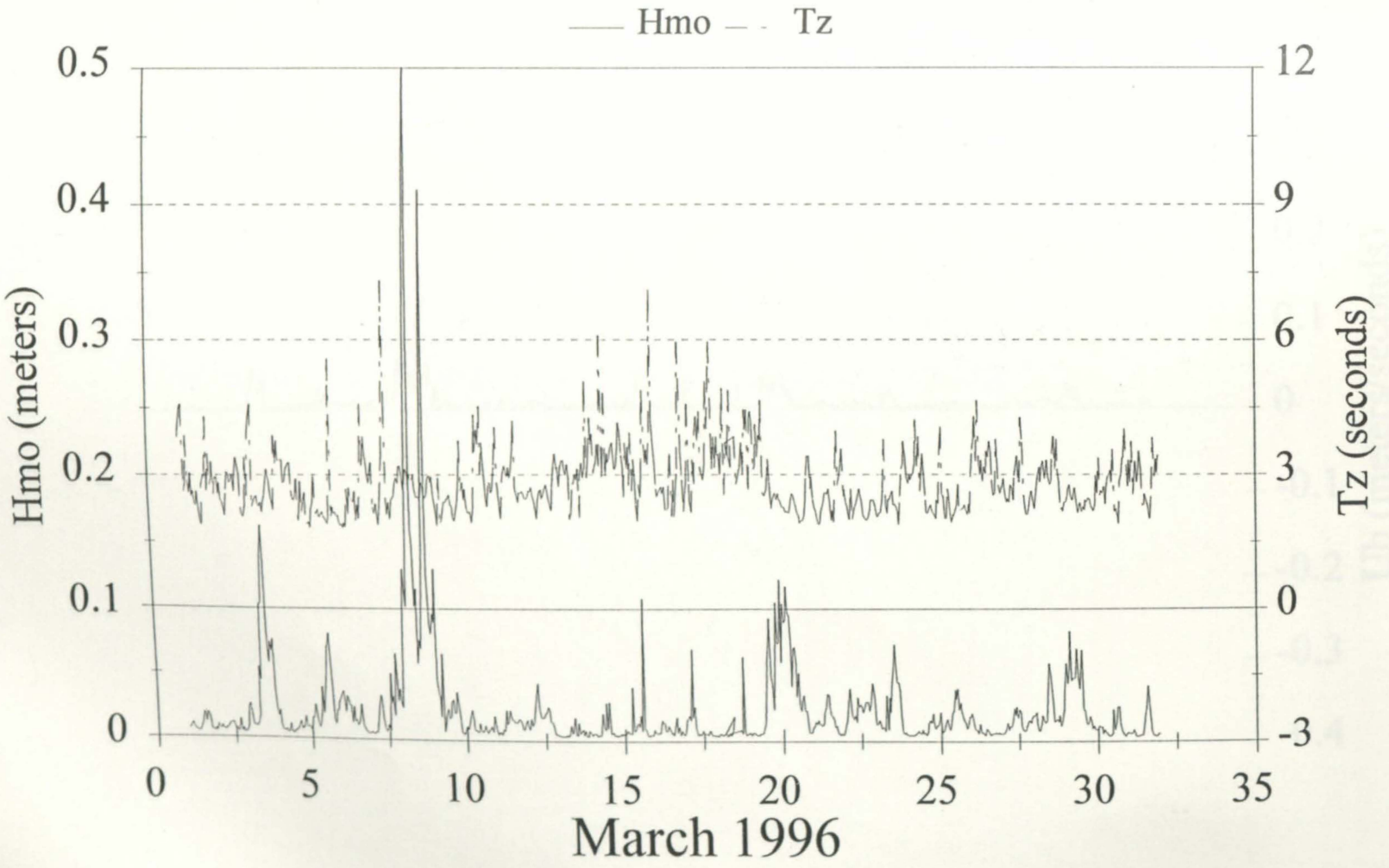

Figure 6

NERRS Catlett Islands Wave Site

Wave Height and Orbital Velocity

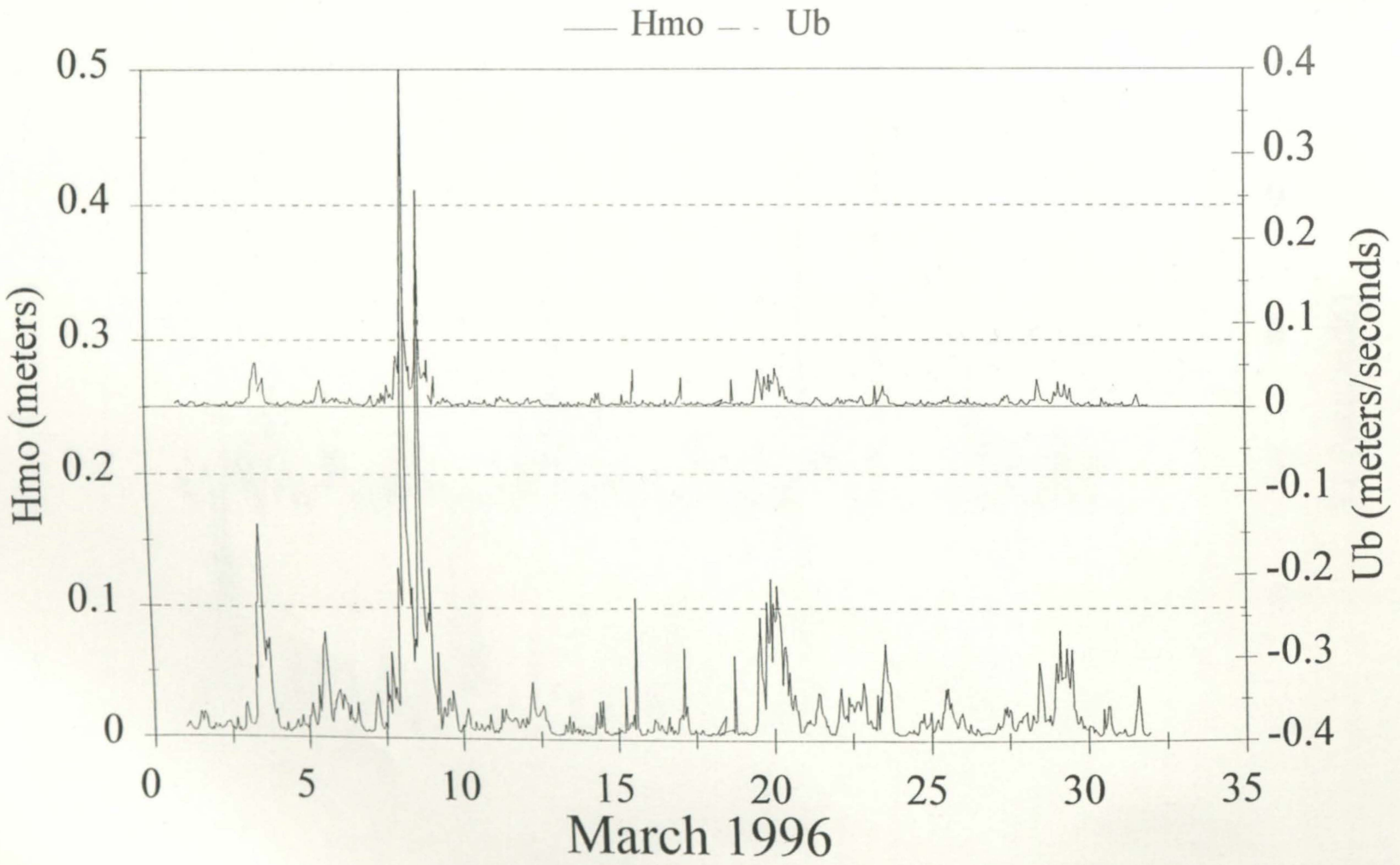

Figure 7

NERRS Catlett Islands Wave Site

Plot of Wave Height and Period

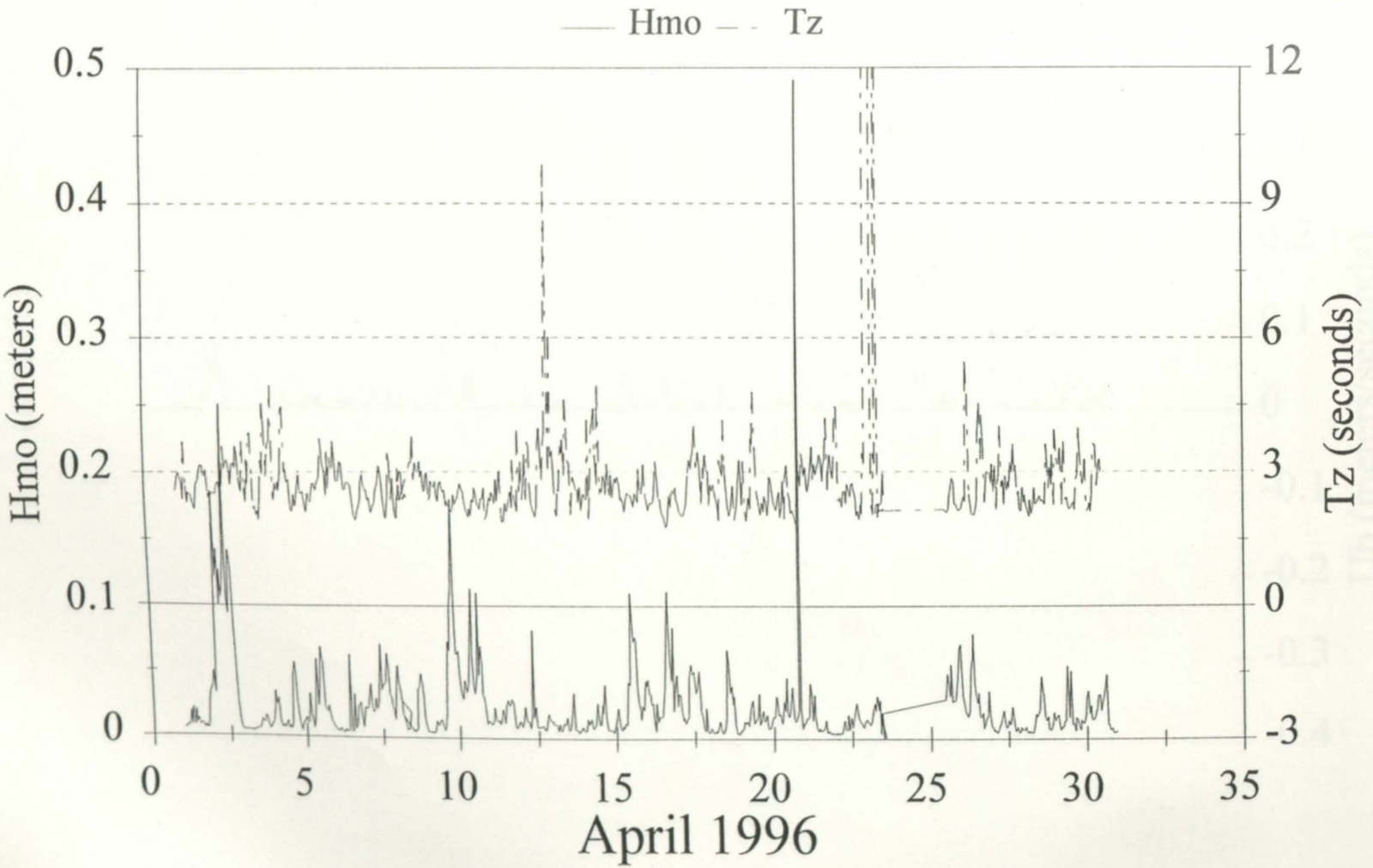

Figure 8

NERRS Catlett Islands Wave Site

Wave Height and Orbital Velocity

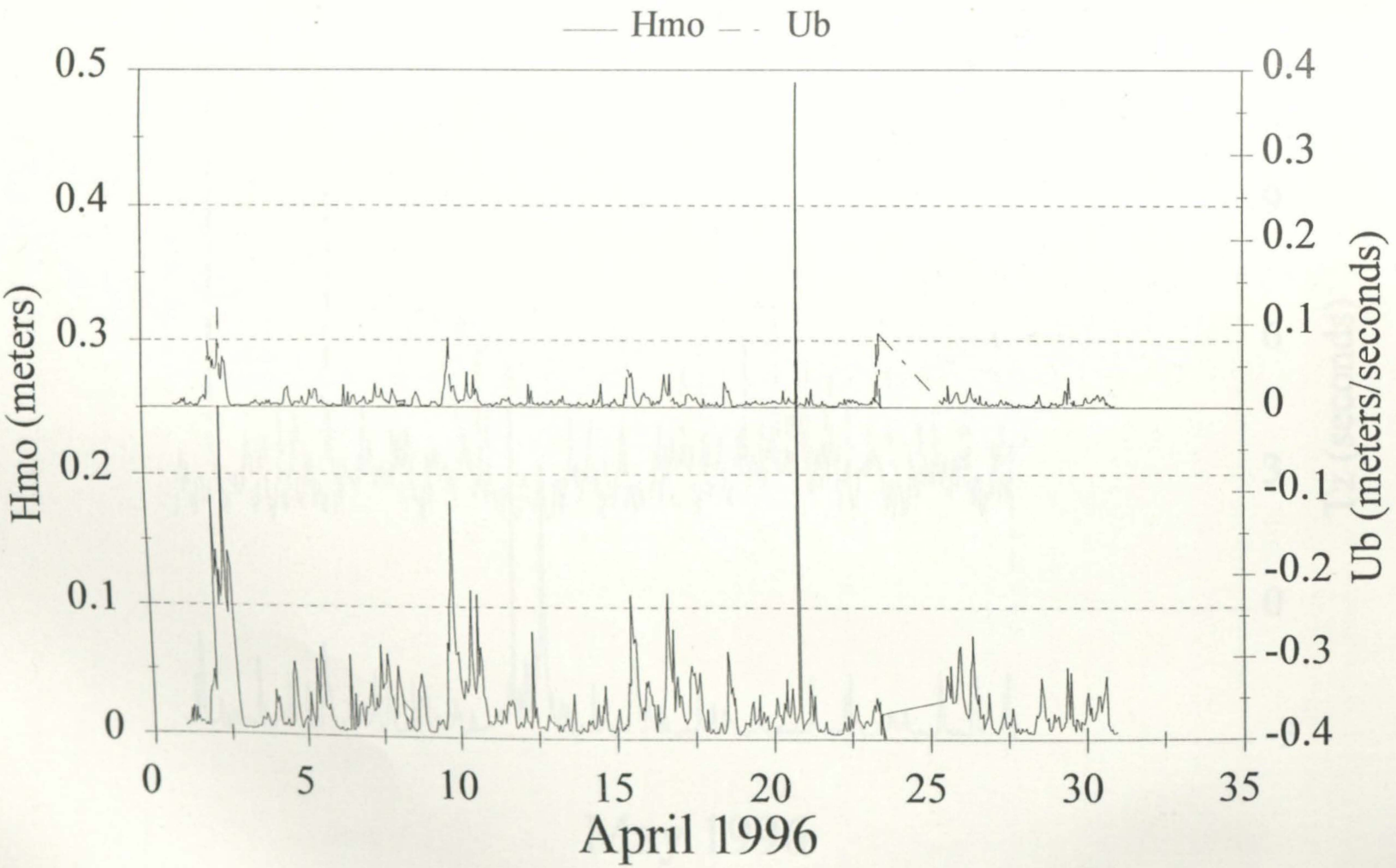

Figure 9

NERRS Catlett Islands Wave Site

Plot of Wave Height and Period

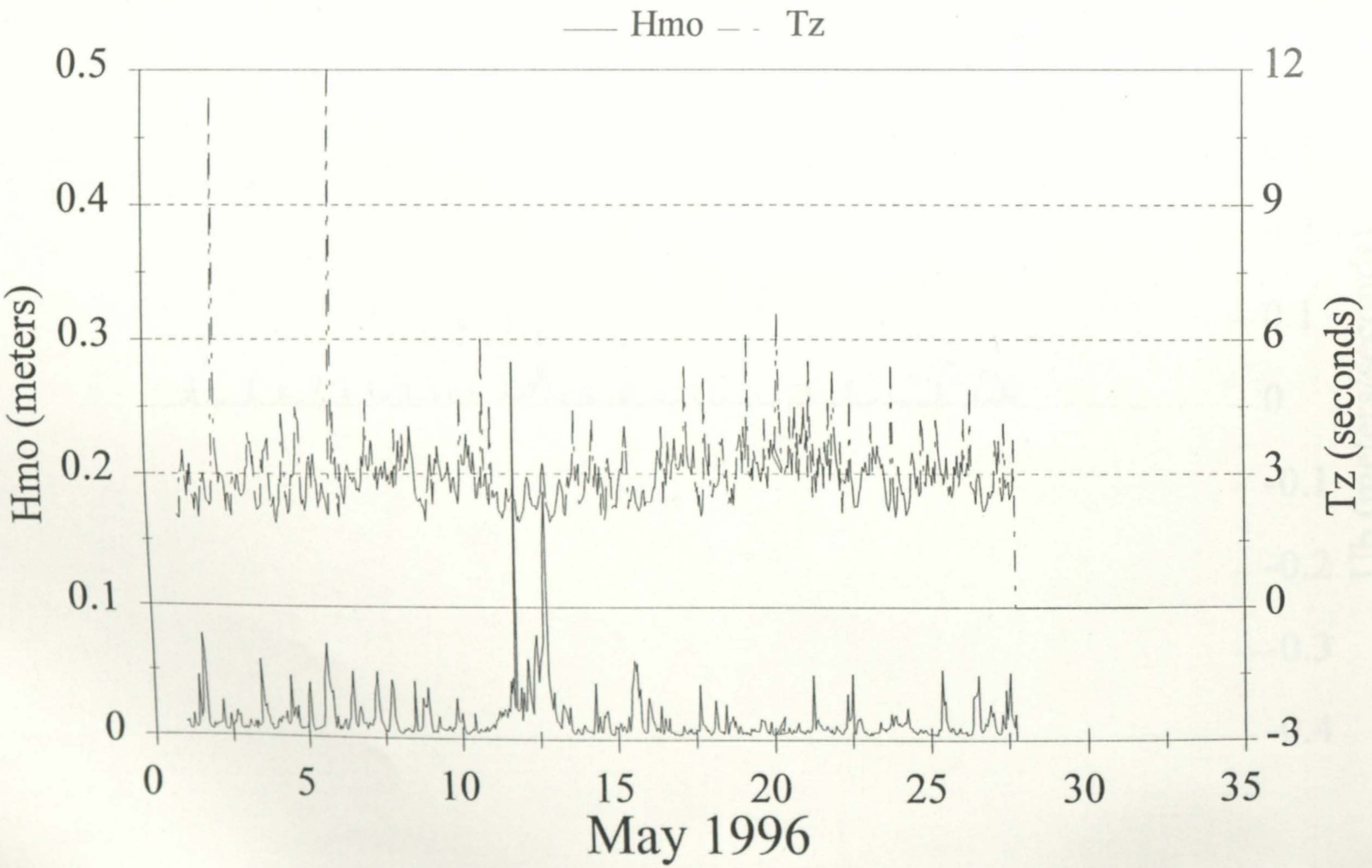

Figure 10

NERRS Catlett Islands Wave Site

Wave Height and Orbital Velocity

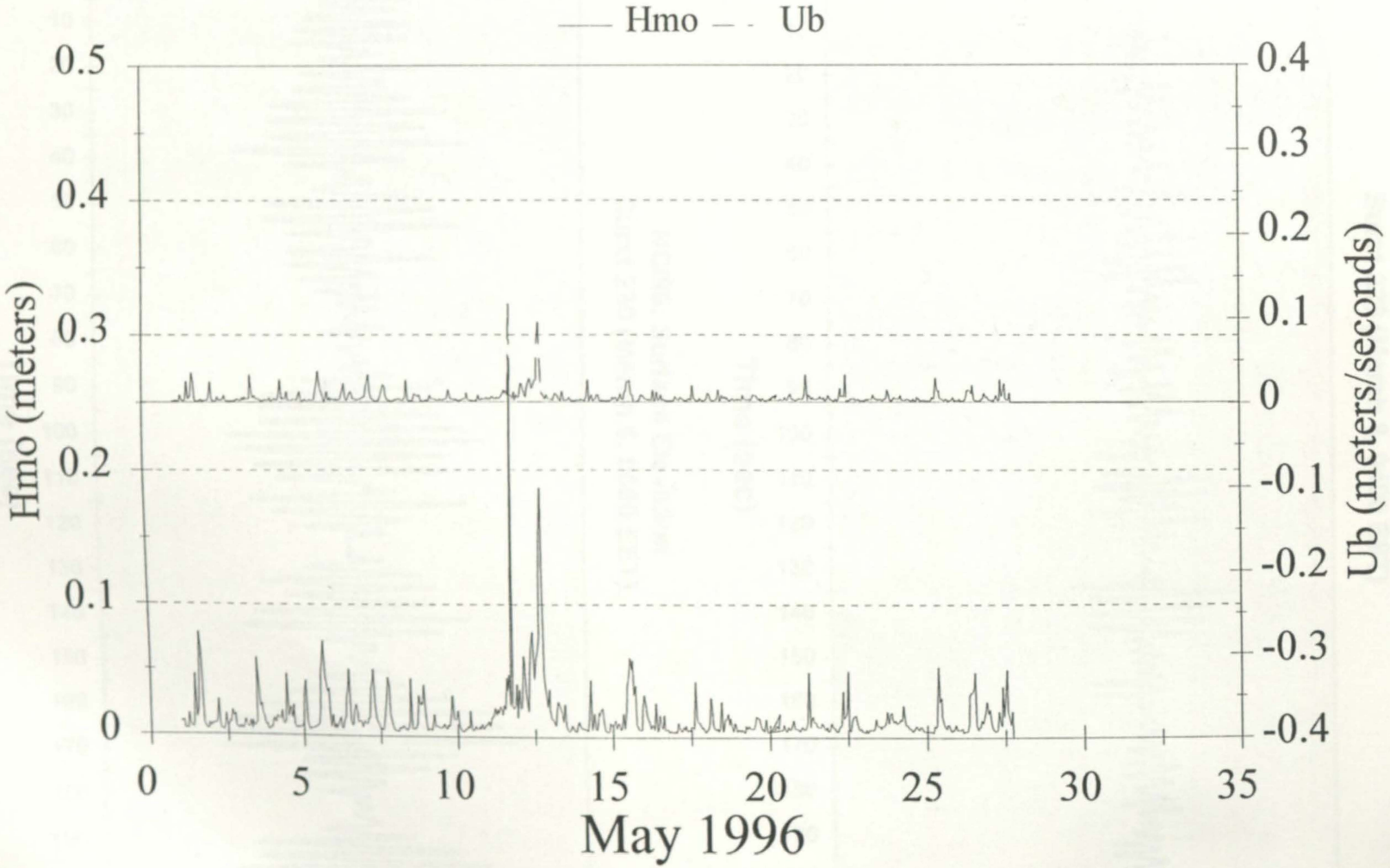

Figure 11

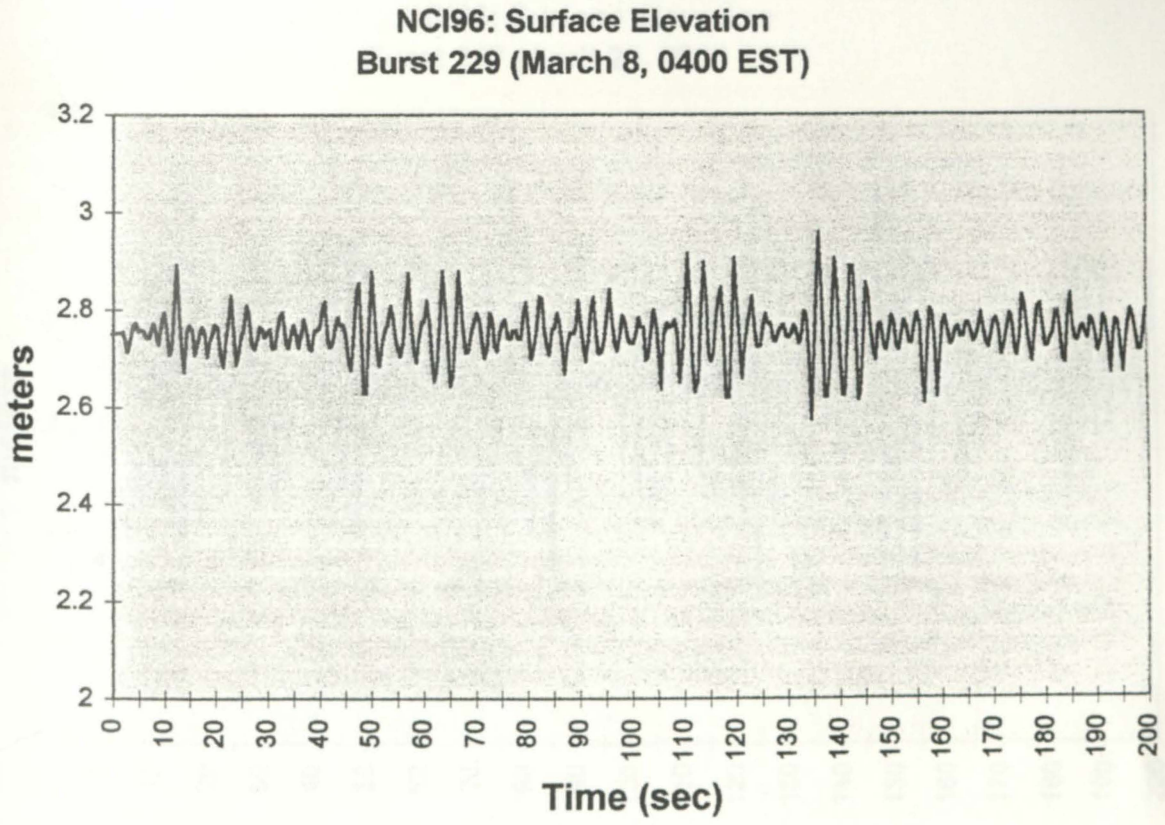
NCI96: Surface Elevation
Burst 229 (March 8, 0400 EST)
meters
3.2
3
2.8
2.6
2.4
2.2
2
0
10
20
30
40
50
60
70
80
90
100
110
120
130
140
150
160
170
180
190
200
Time (sec)

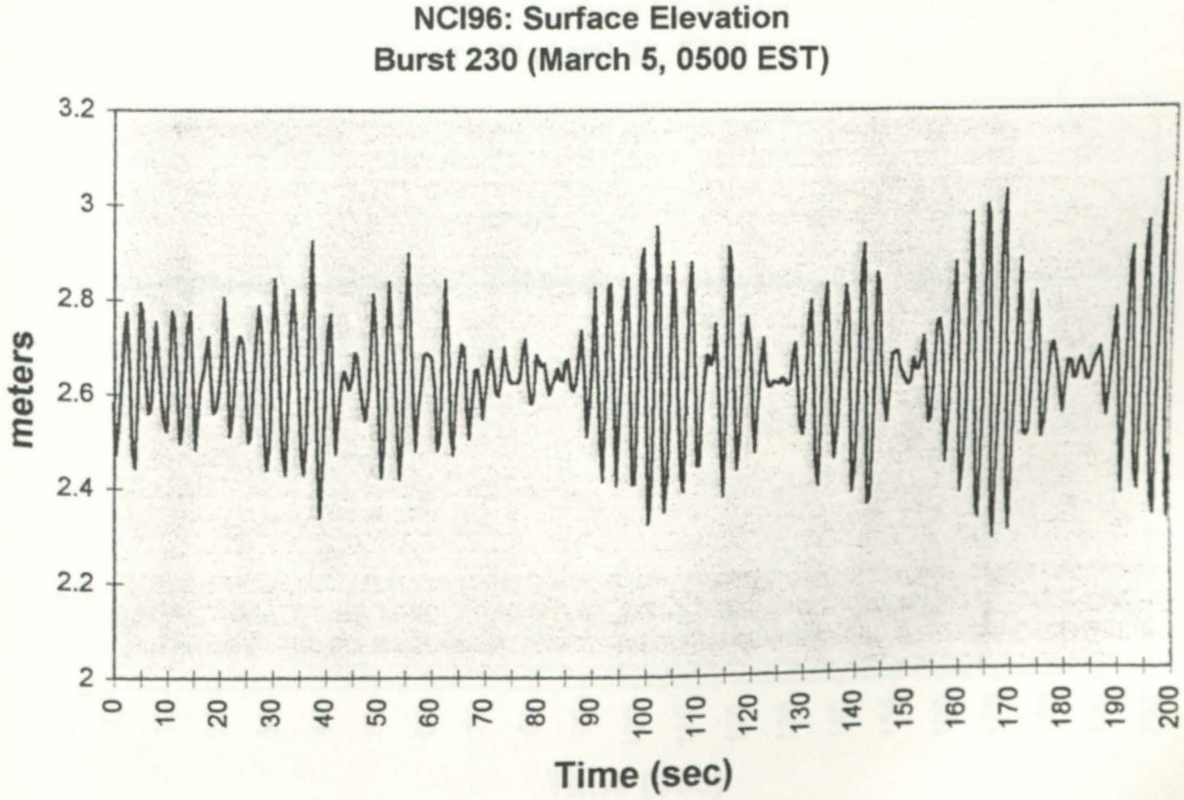
NCI96: Surface Elevation
Burst 230 (March 5, 0500 EST)
meters
3.2
3
2.8
2.6
2.4
2.2
2
0
10
20
30
40
50
60
70
80
90
100
110
120
130
140
150
160
170
180
190
200
Time (sec)

Figure 12

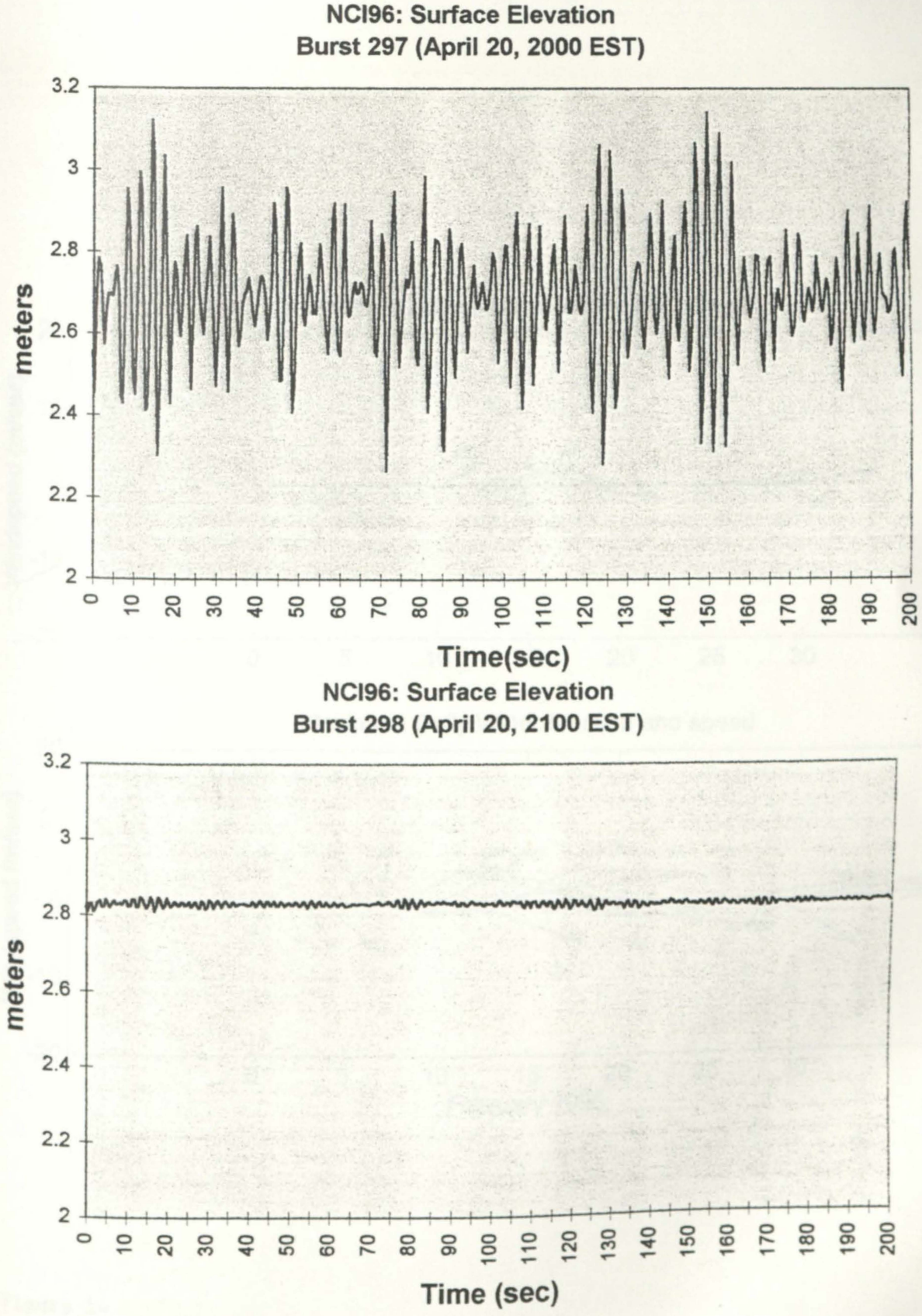
NCI96: Surface Elevation
Burst 297 (April 20, 2000 EST)
meters
3.2
3
2.8
2.6
2.4
2.2
2
0 10 20 30 40 50 60 70 80 90 100 110 120 130 140 150 160 170 180 190 200
Time(sec)
NCI96: Surface Elevation
Burst 298 (April 20, 2100 EST)
meters
3.2
3
2.8
2.6
2.4
2.2
2
0 10 20 30 40 50 60 70 80 90 100 110 120 130 140 150 160 170 180 190 200
Time (sec)

Figure 13

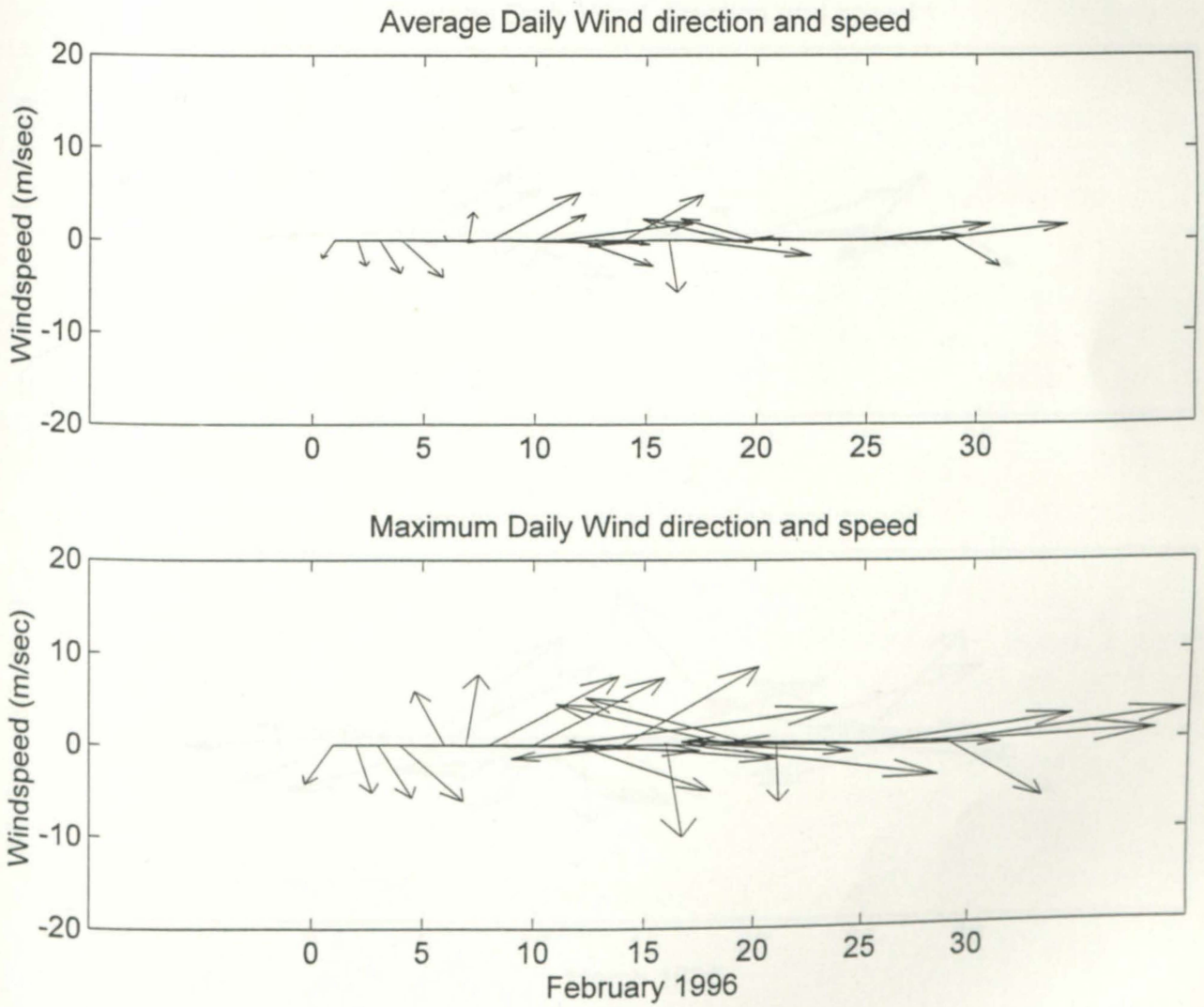
Average Daily Wind direction and speed
Windspeed (m/sec)
20
10
0
-10
-20
0
5
10
15
20
25
30
Maximum Daily Wind direction and speed
Windspeed (m/sec)
20
10
0
-10
-20
0
5
10
15
20
25
30
February 1996

Figure 14

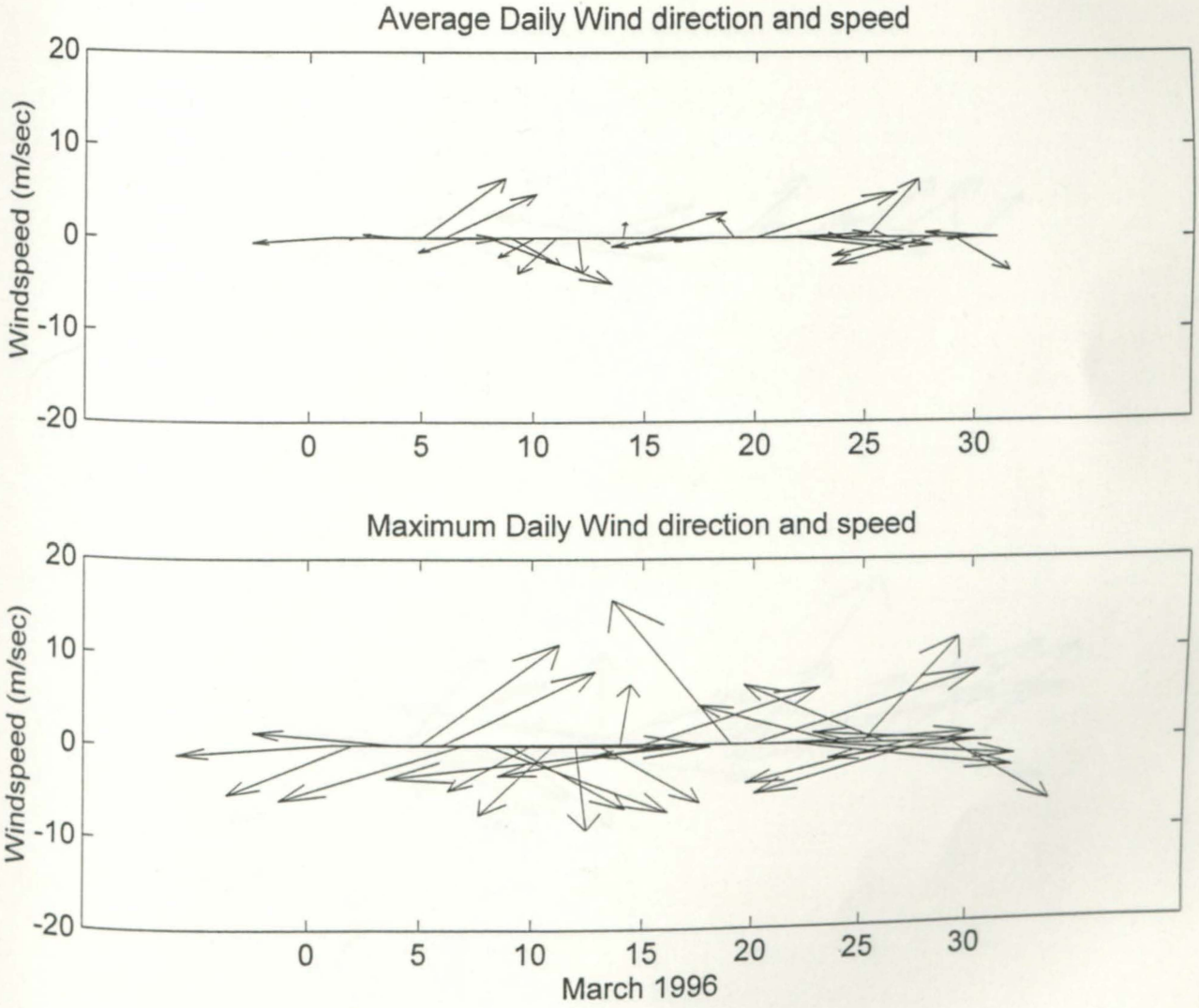
Average Daily Wind direction and speed
Windspeed (m/sec)
20
10
0
-10
-20
0
5
10
15
20
25
30
Maximum Daily Wind direction and speed
Windspeed (m/sec)
20
10
0
-10
-20
0
5
10
15
20
25
30
March 1996

Figure 15

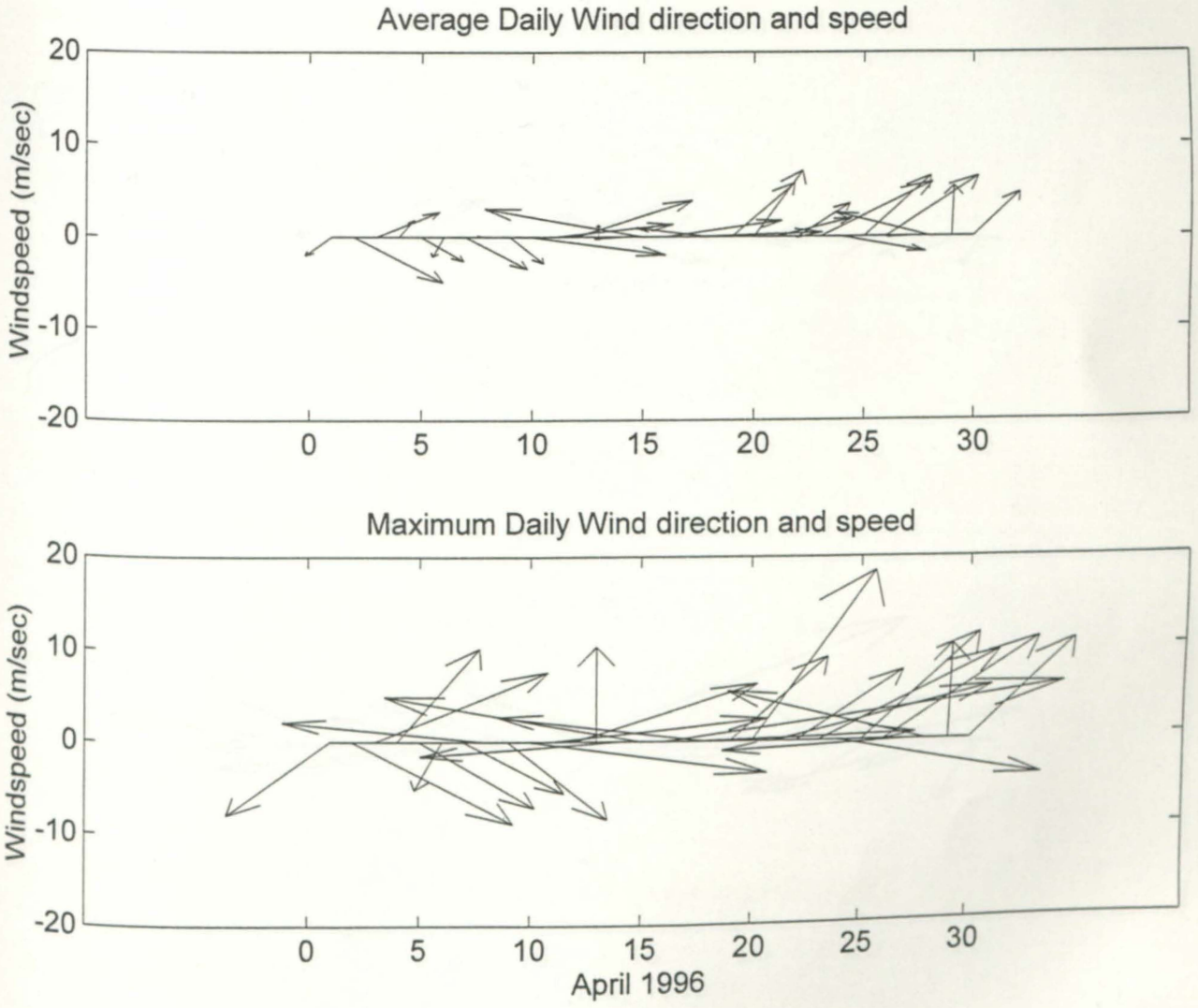
Average Daily Wind direction and speed
Windspeed (m/sec)
20
10
0
-10
-20
0
5
10
15
20
25
30
Maximum Daily Wind direction and speed
Windspeed (m/sec)
20
10
0
-10
-20
0
5
10
15
20
25
30
April 1996

Figure 16

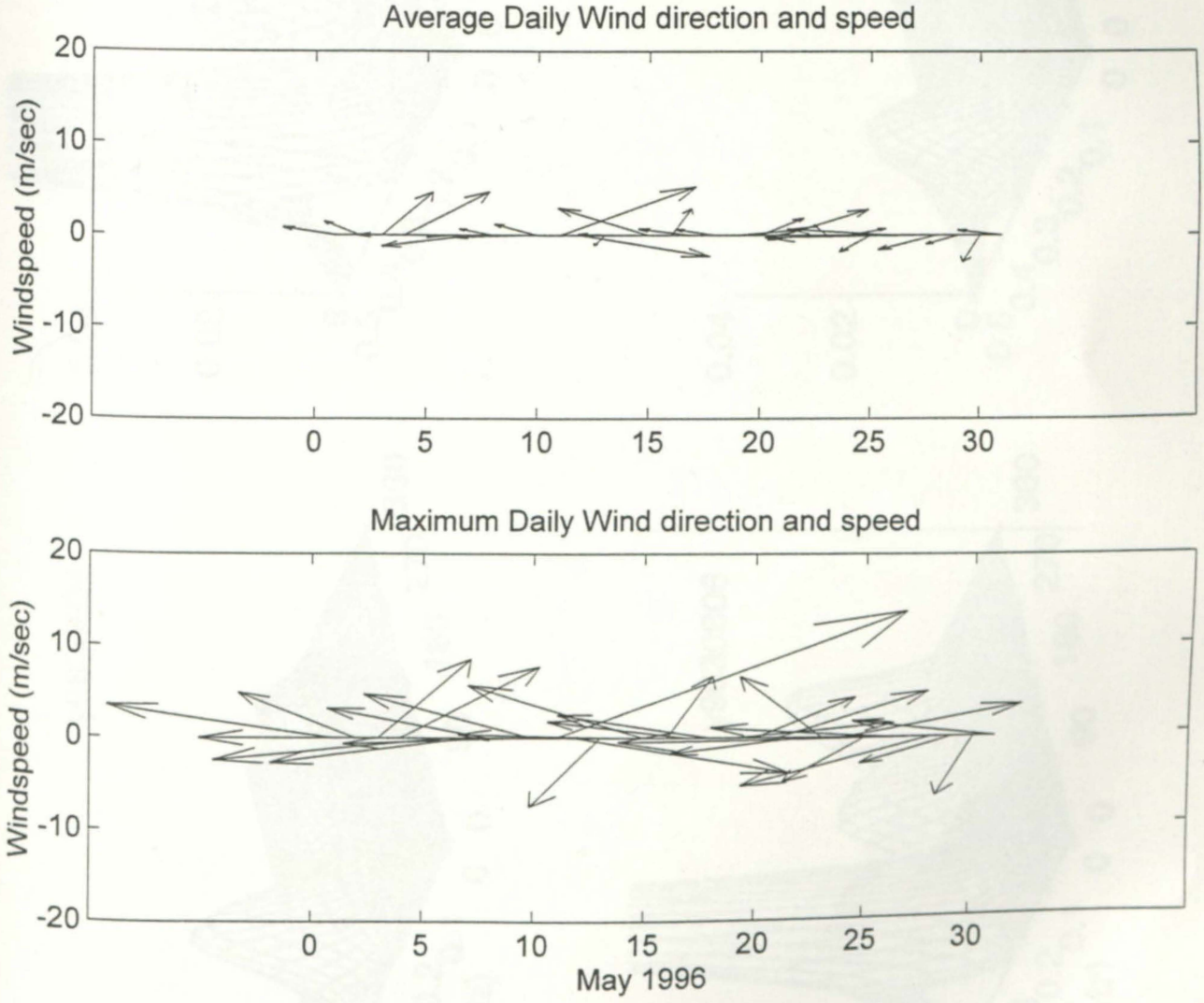
Average Daily Wind direction and speed
Windspeed (m/sec)
20
10
0
-10
-20
0
5
10
15
20
25
30
Maximum Daily Wind direction and speed
Windspeed (m/sec)
20
10
0
-10
-20
0
5
10
15
20
25
30
May 1996

Figure 17

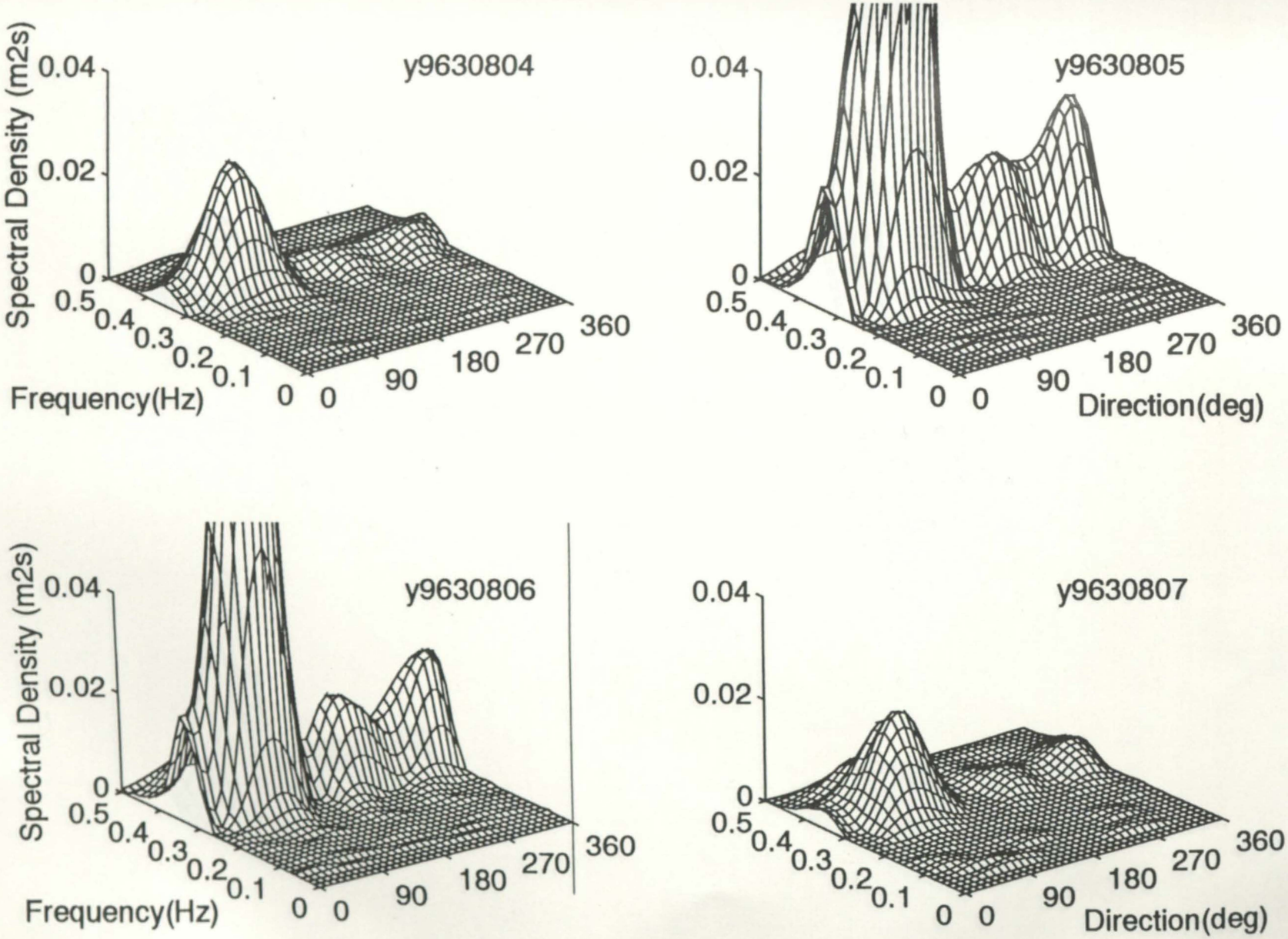
y9630804
Spectral Density (m2s)
0.04
0.02
0
0.5
0.4
0.3
0.2
0.1
Frequency(Hz)
0
0
90
180
270
360
y9630805
Direction(deg)
y9630806
y9630807

Figure 18

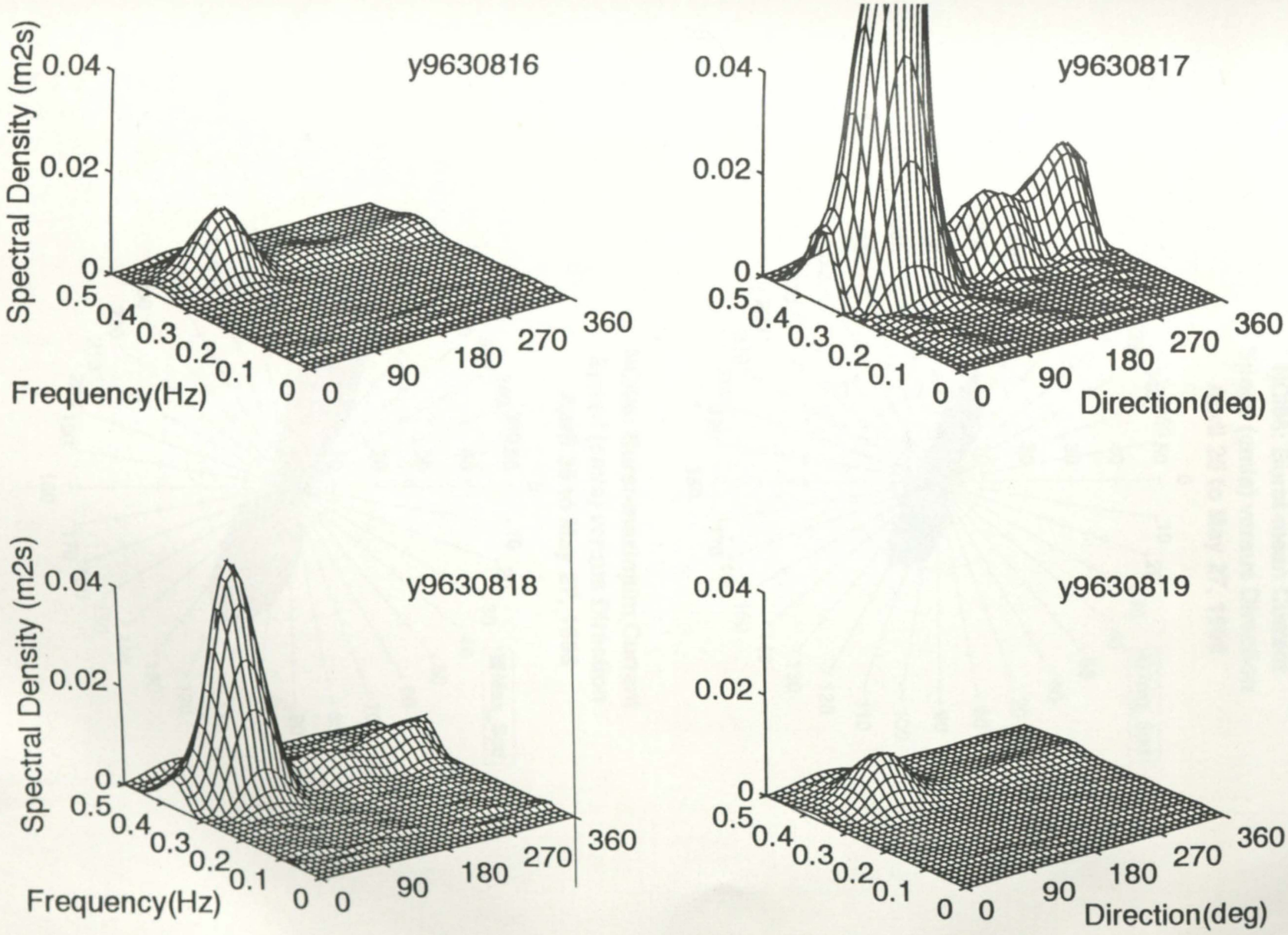
y9630816
Spectral Density (m2s)
0.04
0.02
0
0.5
0.4
0.3
0.2
0.1
0
Frequency(Hz)
0
90
180
270
360
y9630817
Direction(deg)
y9630818
y9630819

Figure 19

NCI96: Burst-mean Current Speed (cm/s) versus Direction April 25 to May 27, 1996

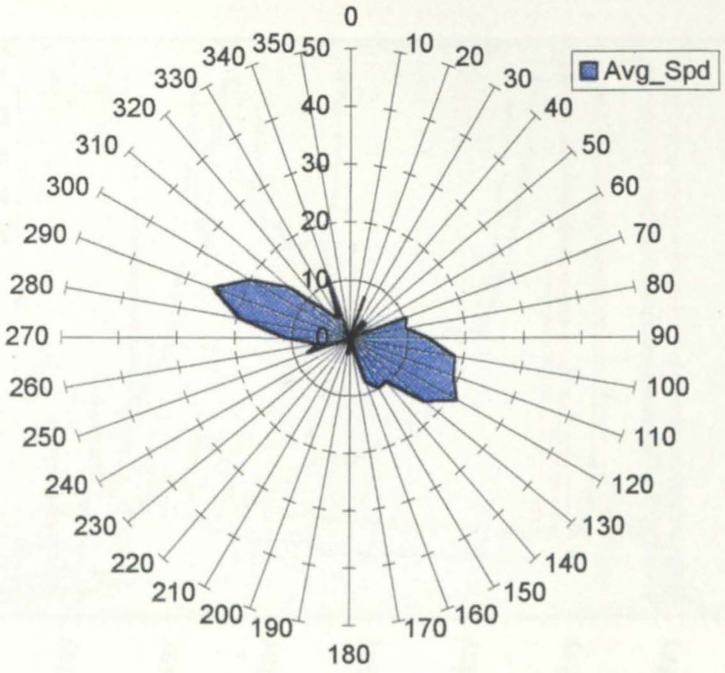

NCI96: Burst-maximum Current Speed (cm/s) versus Direction April 25 to May 27, 1996

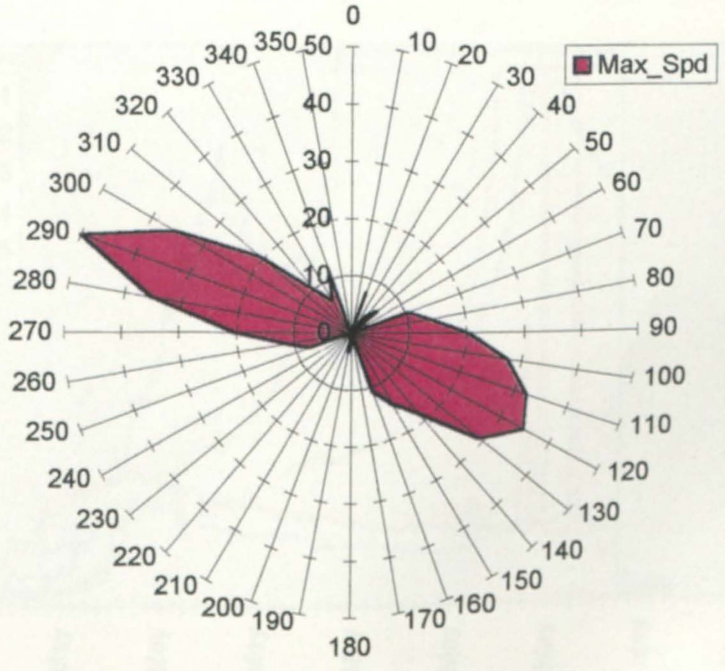

Figure 20

NCI96: Burst-maximum Suspended Sediment Concentration

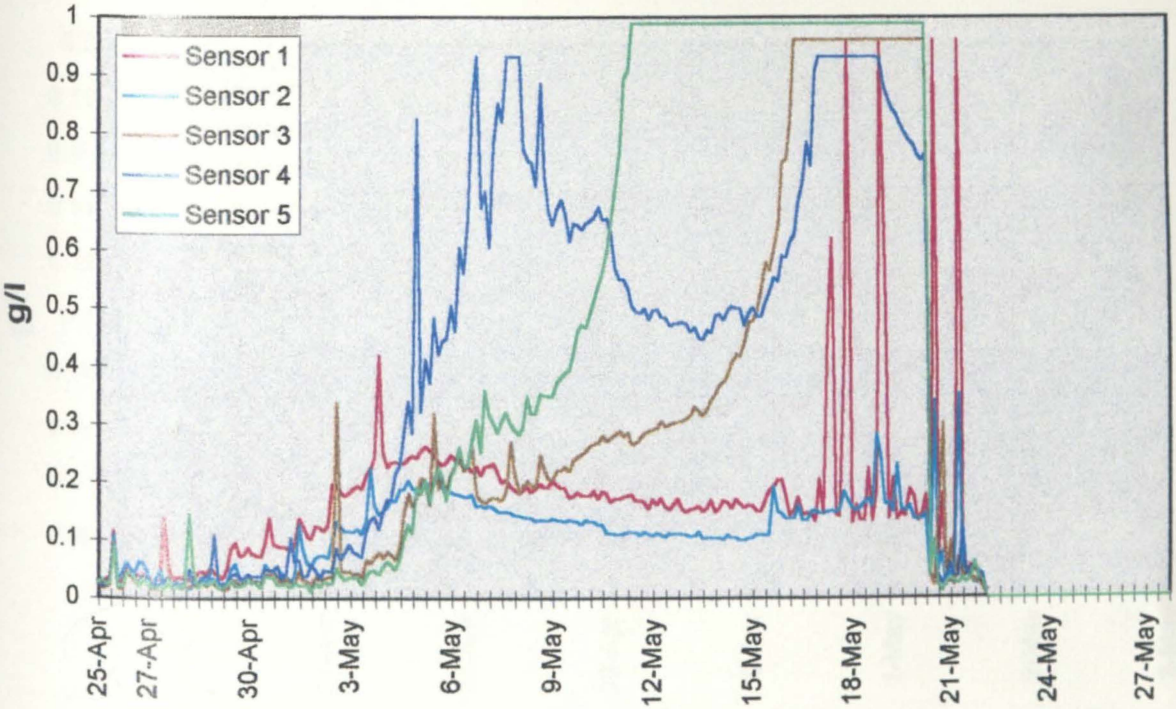

NCI96: Burst-minimum Suspended Sediment concentration

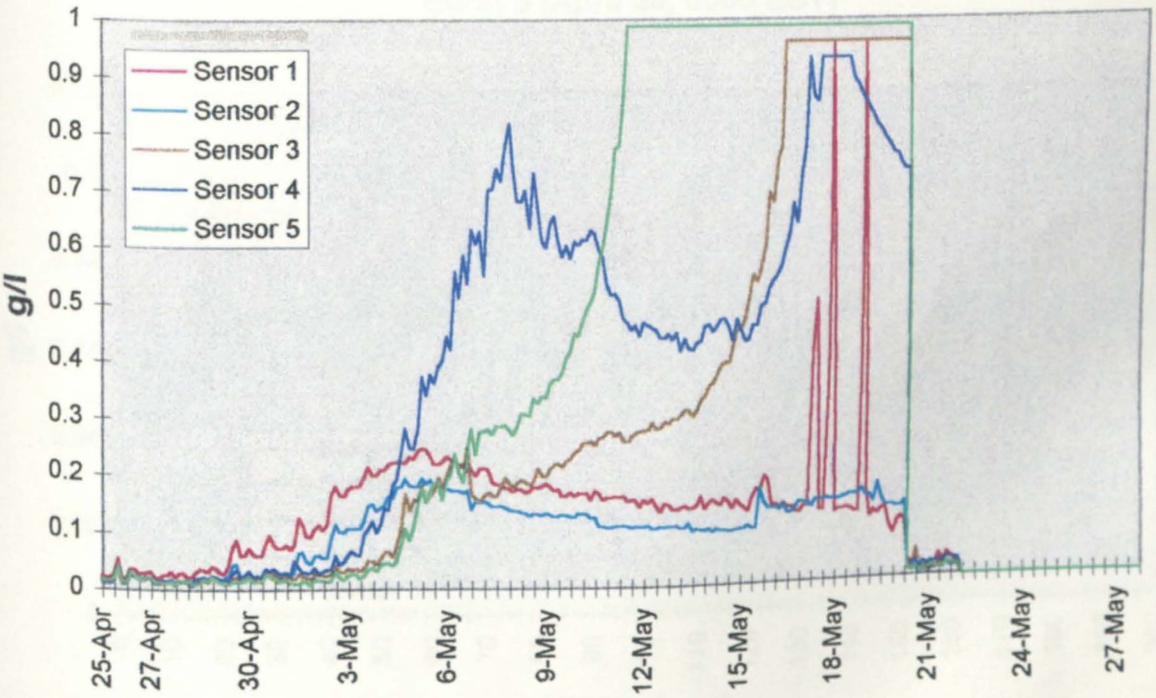

Figure 21

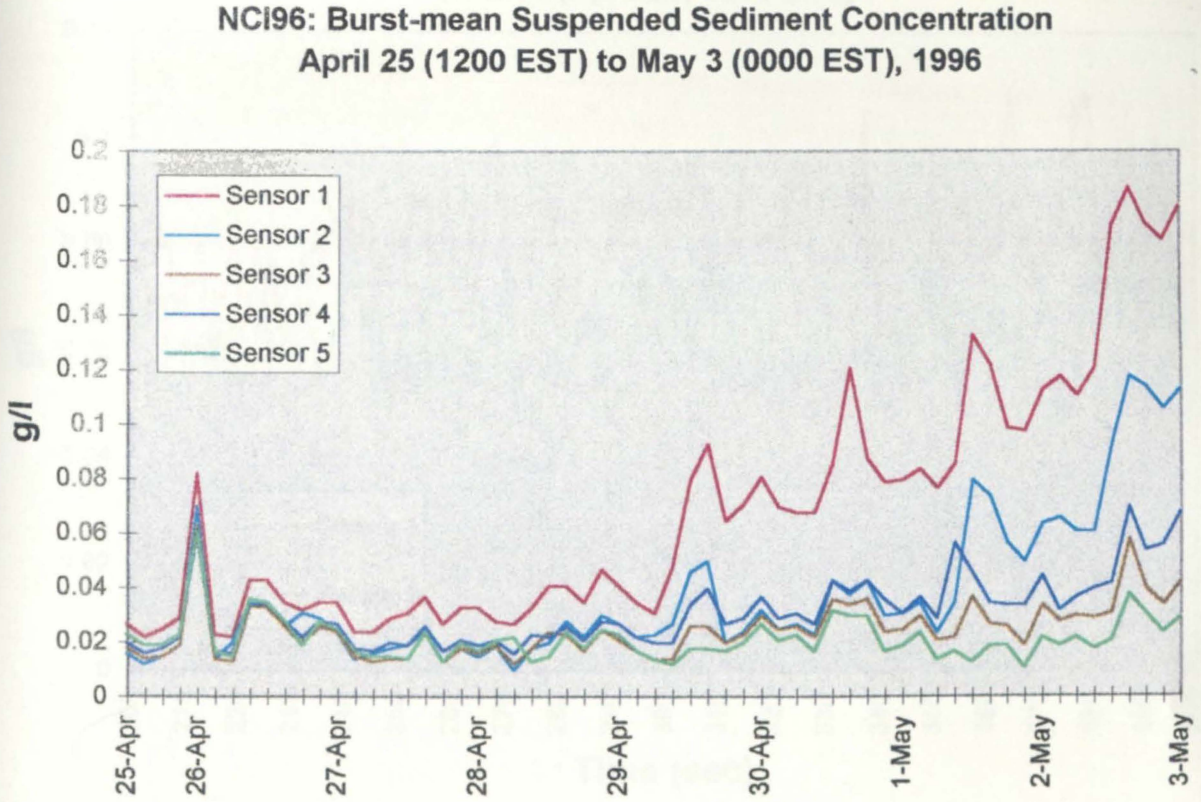
NCI96: Burst-mean Suspended Sediment Concentration
April 25 (1200 EST) to May 3 (0000 EST), 1996
g/l
0.2
0.18
0.16
0.14
0.12
0.1
0.08
0.06
0.04
0.02
0
Sensor 1
Sensor 2
Sensor 3
Sensor 4
Sensor 5
25-Apr
26-Apr
27-Apr
28-Apr
29-Apr
30-Apr
1-May
2-May
3-May

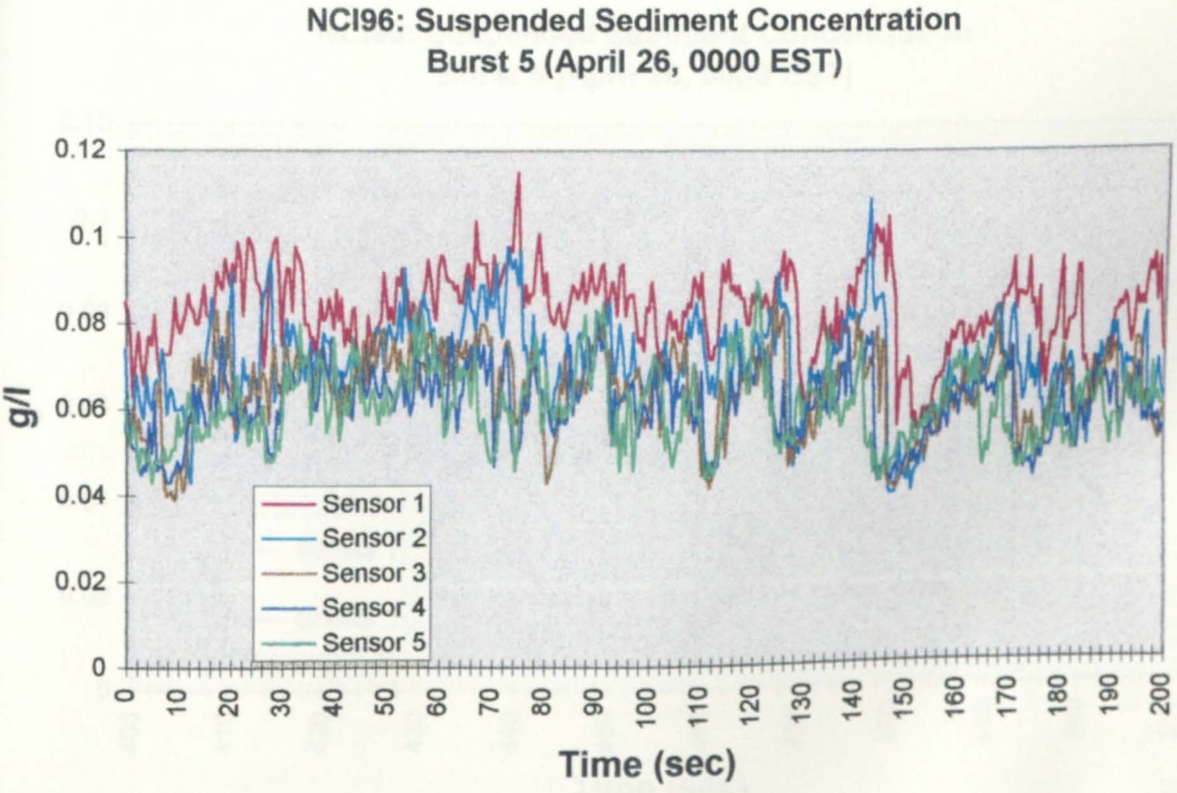
NCI96: Suspended Sediment Concentration
Burst 5 (April 26, 0000 EST)
g/l
0.12
0.1
0.08
0.06
0.04
0.02
0
Sensor 1
Sensor 2
Sensor 3
Sensor 4
Sensor 5
0
10
20
30
40
50
60
70
80
90
100
110
120
130
140
150
160
170
180
190
200
Time (sec)

Figure 22

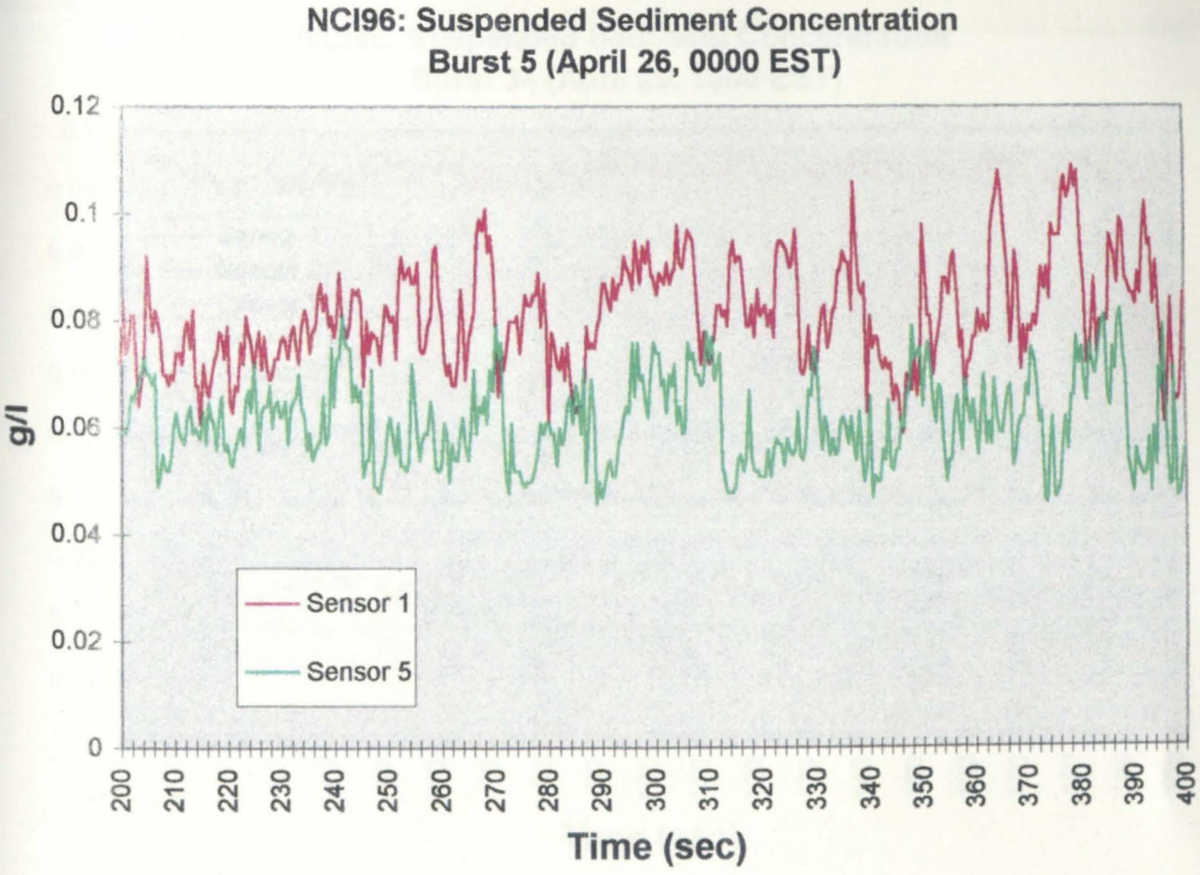
NCI96: Suspended Sediment Concentration
Burst 5 (April 26, 0000 EST)
g/l
0.12
0.1
0.08
0.06
0.04
0.02
0
Sensor 1
Sensor 5
200
210
220
230
240
250
260
270
280
290
300
310
320
330
340
350
360
370
380
390
400
Time (sec)

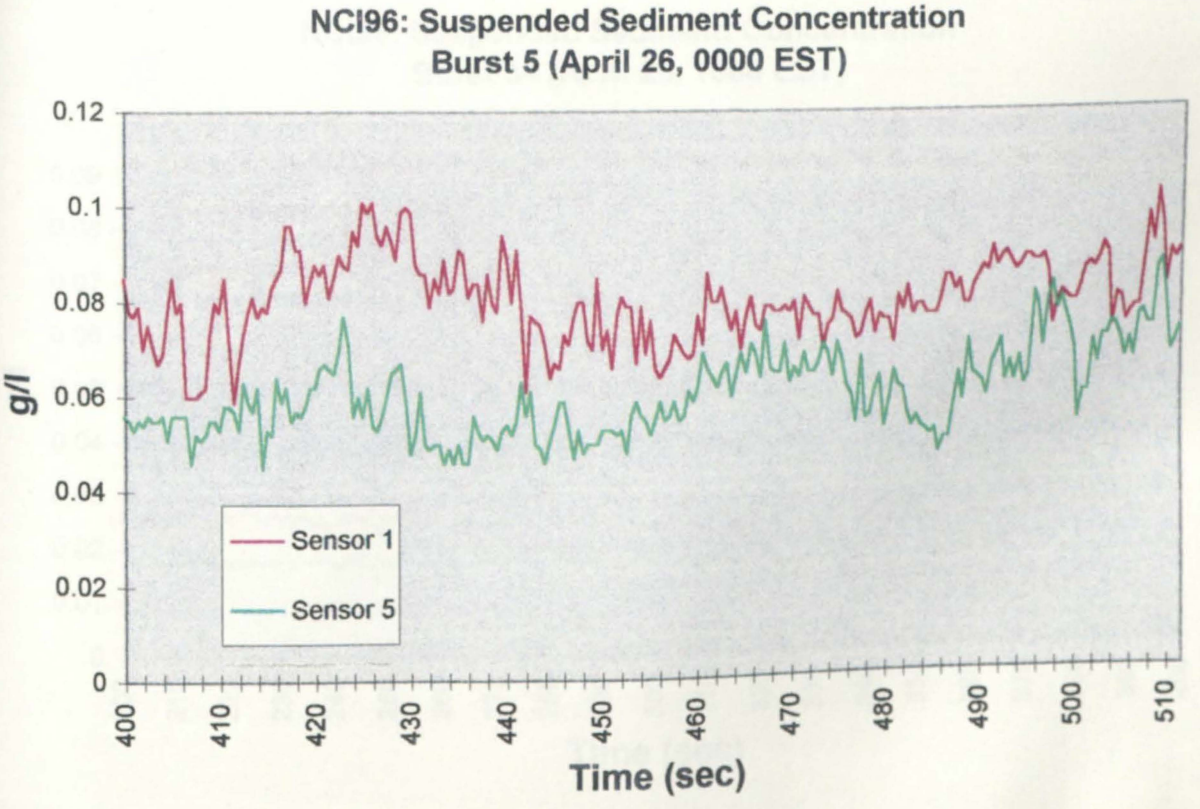
NCI96: Suspended Sediment Concentration
Burst 5 (April 26, 0000 EST)
g/l
0.12
0.1
0.08
0.06
0.04
0.02
0
Sensor 1
Sensor 5
400
410
420
430
440
450
460
470
480
490
500
510
Time (sec)

Figure 23

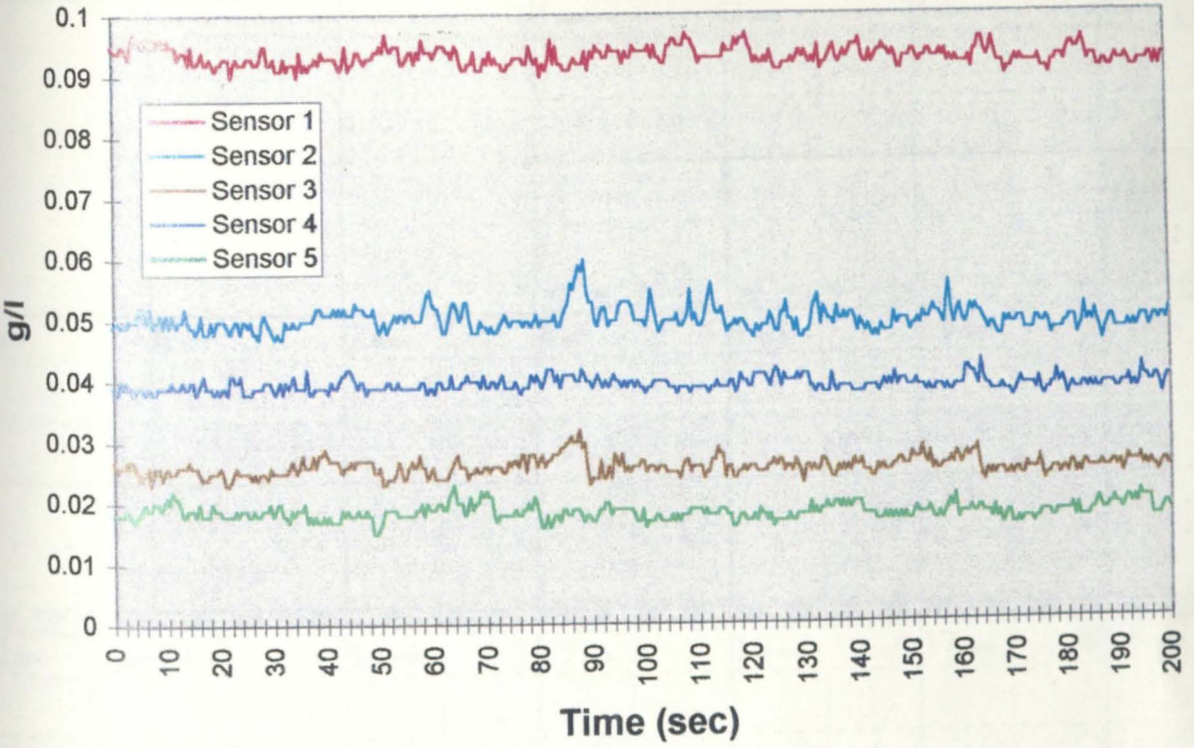
NCI96: Suspended Sediment Concentration
Burst 34 (April 29, 1500 EST)
g/l
Time (sec)
Sensor 1
Sensor 2
Sensor 3
Sensor 4
Sensor 5
0.1
0.09
0.08
0.07
0.06
0.05
0.04
0.03
0.02
0.01
0
0 10 20 30 40 50 60 70 80 90 100 110 120 130 140 150 160 170 180 190 200

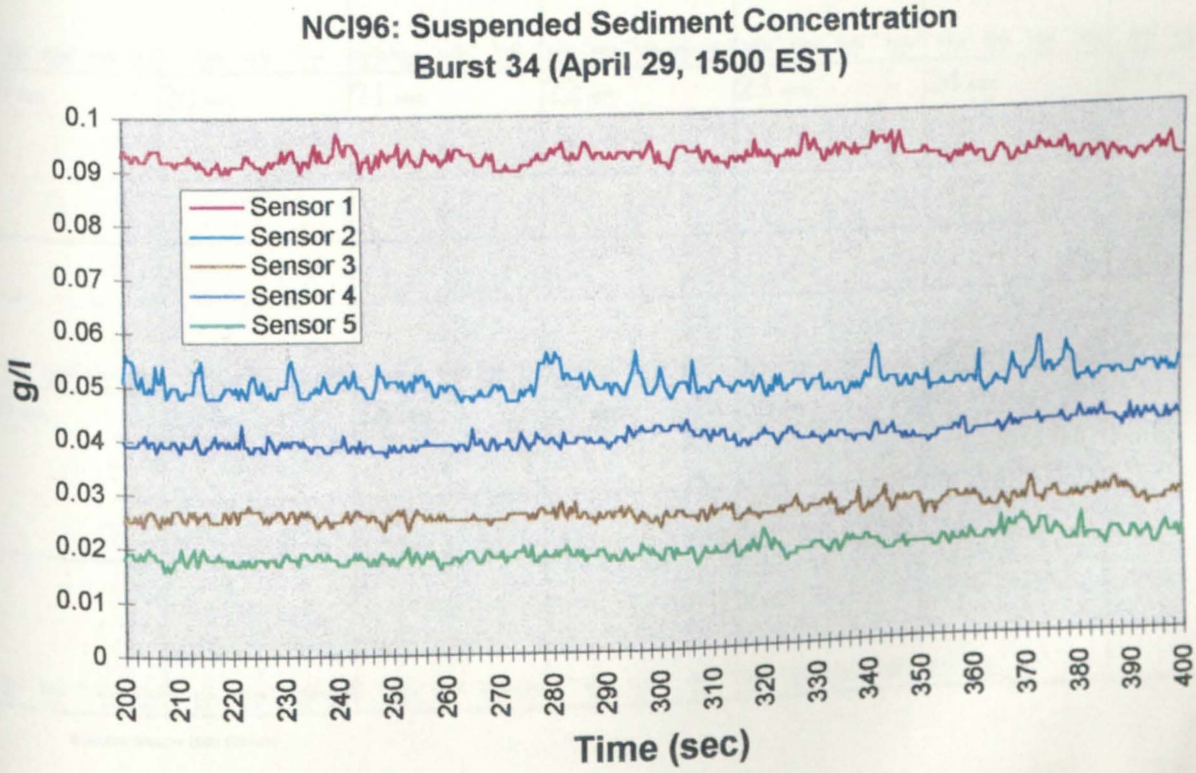
NCI96: Suspended Sediment Concentration
Burst 34 (April 29, 1500 EST)
g/l
Time (sec)
Sensor 1
Sensor 2
Sensor 3
Sensor 4
Sensor 5
0.1
0.09
0.08
0.07
0.06
0.05
0.04
0.03
0.02
0.01
0
200 210 220 230 240 250 260 270 280 290 300 310 320 330 340 350 360 370 380 390 400

Figure 24

Currents-Pages Rock, 1 mile SSE of

based on C40 - Chesapeake Bay Entrance (NOAA)
37° 17.06 N 76° 34.08 W

May 1996

Average Currents
Min Before Flood: -- --
Avg Max Flood: 1.0 kt 303°
Min Before Ebb: -- --
Avg Max Ebb: 1.0 kt 125°

Monthly Max Flood & Ebb
Flood May 4, 10:11p 1.7 kt
Ebb May 4, 3:34p 1.3 kt

Sunday	Monday	Tuesday	Wednesday	Thursday	Friday	Saturday
			1 (EDT) 1:15a -1.0, 7:34a 0.9, 1:21p -1.1, 8:05p 1.4	2 (EDT) 2:03a -1.1, 8:16a 1.0, 2:00p -1.2, 8:45p 1.5, 11:28p -0.1	3 (EDT) 2:48a -1.2, 9:02a 1.0, 2:50p -1.3, 9:27p 1.6	4 (EDT) 3:33a -1.3, 9:49a 1.0, 3:34p -1.3, 10:11p 1.7
5 (EDT) 4:18a -1.3, 10:36a 1.0, 4:20p -1.3, 10:56p 1.7	6 (EDT) 5:07a -1.3, 11:24a 1.0, 5:11p -1.2, 11:45p 1.6	7 (EDT) 6:04a -1.2, 12:19p 0.9, 6:11p -1.1	8 (EDT) 12:40a 1.4, 7:05a -1.2, 1:19p 0.9, 7:17p -1.0	9 (EDT) 1:39a 1.3, 8:04a -1.1, 2:22p 0.8, 8:22p -1.0	10 (EDT) 2:40a 1.1, 9:04a -1.1, 3:29p 0.8, 9:33p -0.9	11 (EDT) 3:46a 0.9, 10:09a -1.1, 4:48p 0.9, 10:47p -1.0
12 (EDT) 5:03a 0.9, 11:09a -1.1, 5:56p 1.1, 11:50p -1.0	13 (EDT) 6:06a 0.9, 12:02p -1.1, 6:43p 1.2	14 (EDT) 12:47a 0.9, 6:58a 0.9, 12:50p -1.1, 7:23p 1.3	15 (EDT) 1:40a -1.2, 7:40a 0.9, 1:36p -1.1, 8:04p 1.4, 11:01p -0.1	16 (EDT) 2:30a -1.2, 8:27a 0.9, 2:20p -1.1, 8:47p 1.4	17 (EDT) 3:14a -1.2, 9:15a 0.9, 2:59p -1.1, 9:30p 1.4	18 (EDT) 3:54a -1.1, 10:00a 0.8, 3:34p -1.1, 10:11p 1.4
19 (EDT) 4:33a -1.1, 10:43a 0.8, 4:08p -1.0, 10:52p 1.3	20 (EDT) 5:12a -1.0, 11:26a 0.7, 4:44p -0.9, 11:33p 1.2	21 (EDT) 5:56a -0.9, 12:13p 0.6, 5:26p -0.8	22 (EDT) 12:18a 1.0, 6:43a -0.8, 1:05p 0.5, 6:17p -0.7	23 (EDT) 1:06a 0.9, 7:26a -0.8, 1:57p 0.5, 7:10p -0.7	24 (EDT) 1:54a 0.7, 8:06a -0.8, 2:49p 0.5, 8:01p -0.6	25 (EDT) 2:41a 0.6, 8:47a -0.8, 3:46p 0.5, 8:55p -0.6
26 (EDT) 3:33a 0.6, 9:34a -0.8, 4:51p 0.6, 9:58p -0.6	27 (EDT) 4:33a 0.6, 10:25a -0.9, 5:39p 0.8, 11:01p -0.7	28 (EDT) 5:29a 0.6, 11:12a -1.0, 6:15p 1.0, 11:53p -0.8	29 (EDT) 6:15a 0.7, 11:57a -1.1, 6:50p 1.2	30 (EDT) 12:43a -1.0, 6:56a 0.8, 12:43p -1.2, 7:29p 1.5	31 (EDT) 1:34a -1.1, 7:42a 0.9, 1:33p -1.3, 8:12p 1.6	

Figure 25

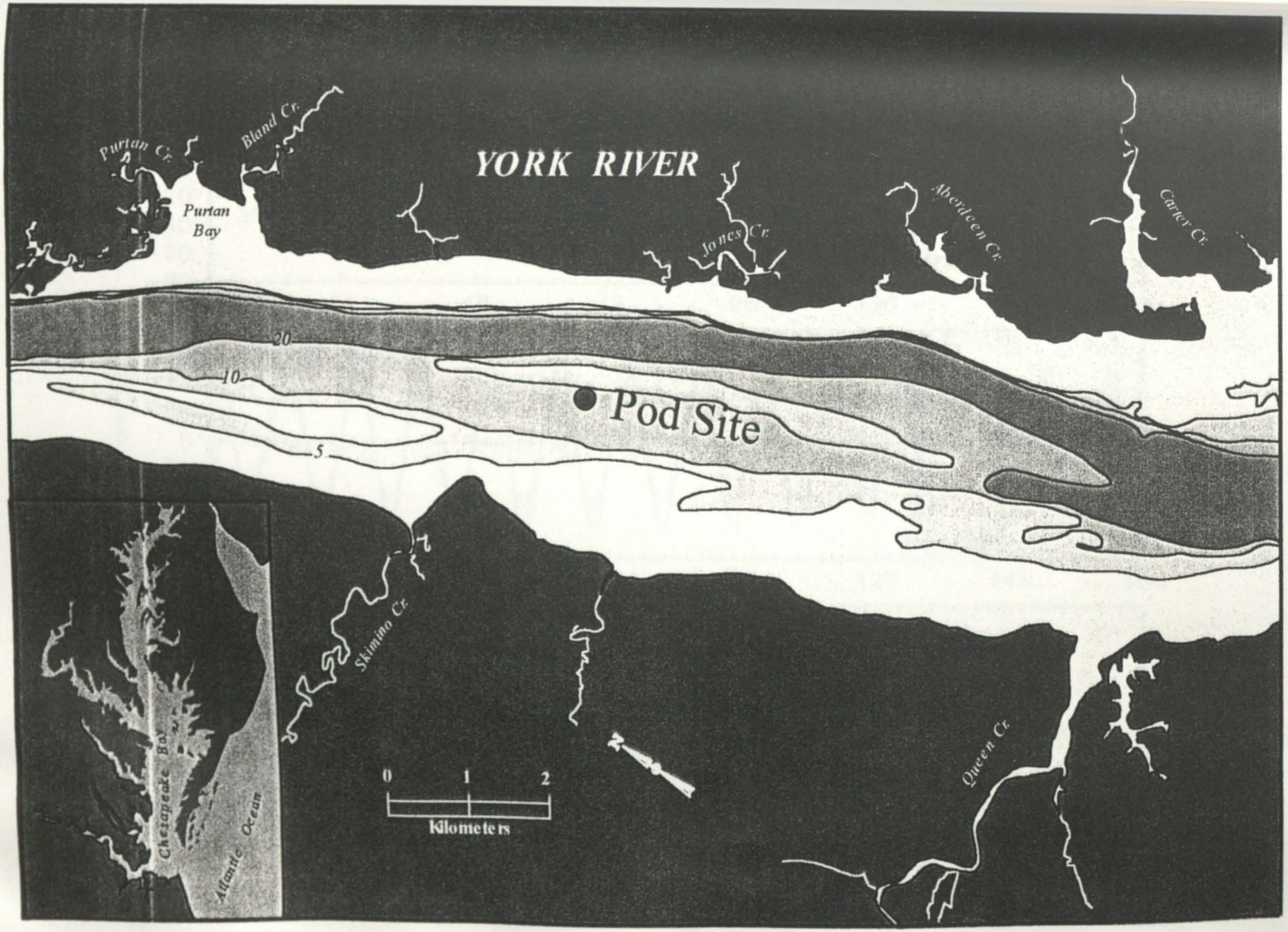
YORK RIVER
Purtan Cr.
Bland Cr.
Purtan Bay
Jones Cr.
Aberdeen Cr.
Carter Cr.
20
10
5
Pod Site
Skimino Cr.
Queen Cr.
0
1
2
Kilometers
Chesapeake Bay
Atlantic Ocean

Figure 26

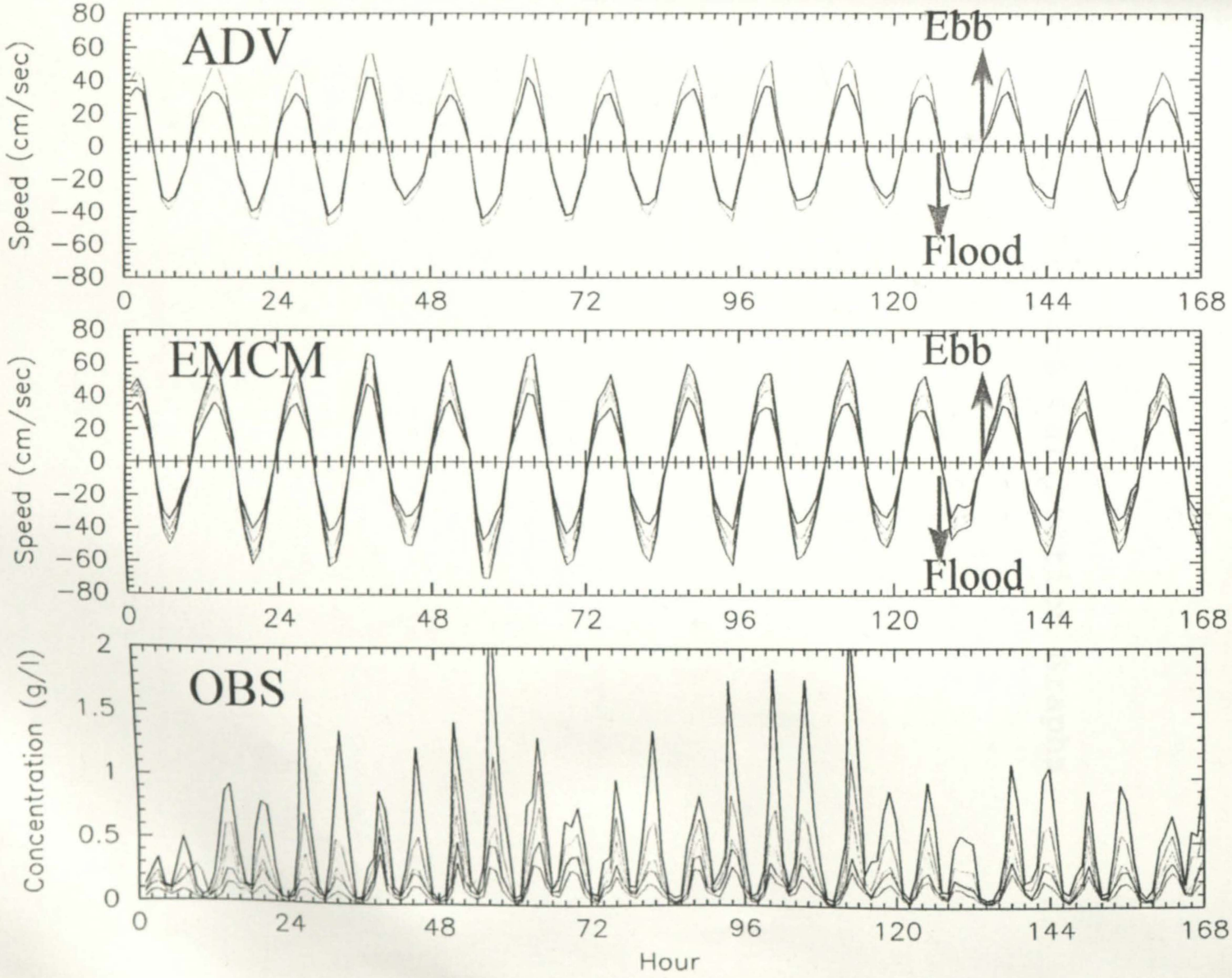
ADV
Ebb
Flood
Speed (cm/sec)
80
60
40
20
0
−20
−40
−60
−80
0
24
48
72
96
120
144
168
EMCM
Ebb
Flood
Speed (cm/sec)
OBS
Concentration (g/l)
2
1.5
1
0.5
0
Hour

Figure 27

IX. OBS Calibration Graphs

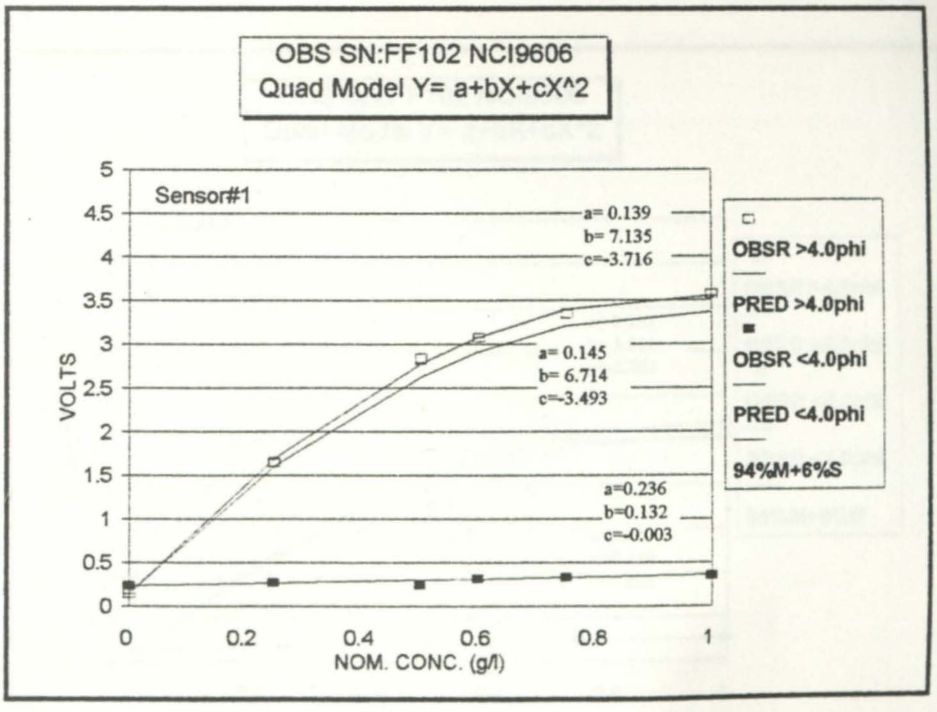
OBS SN:FF102 NCI9606
Quad Model Y= a+bX+cX^2
Sensor#1
a= 0.139
b= 7.135
c=-3.716
a= 0.145
b= 6.714
c=-3.493
a=0.236
b=0.132
c=-0.003
OBSR >4.0phi
PRED >4.0phi
OBSR <4.0phi
PRED <4.0phi
94%M+6%S
VOLTS
NOM. CONC. (g/l)
0
0.5
1
1.5
2
2.5
3
3.5
4
4.5
5
0.2
0.4
0.6
0.8

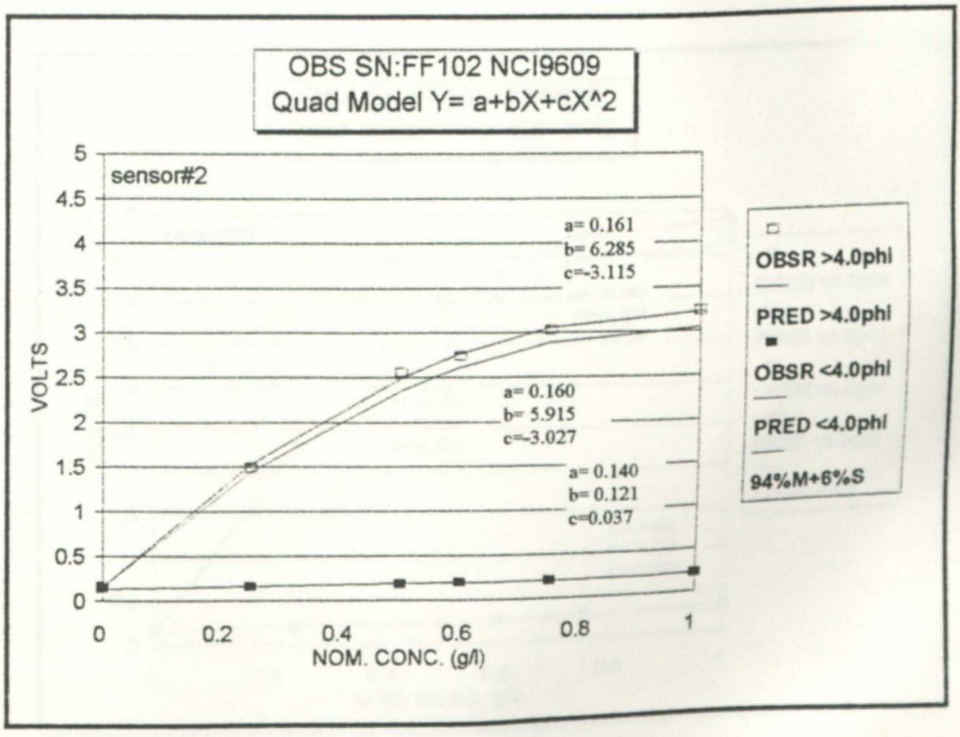
OBS SN:FF102 NCI9609
Quad Model Y= a+bX+cX^2
sensor#2
a= 0.161
b= 6.285
c=-3.115
a= 0.160
b= 5.915
c=-3.027
a= 0.140
b= 0.121
c=0.037
OBSR >4.0phi
PRED >4.0phi
OBSR <4.0phi
PRED <4.0phi
94%M+6%S
VOLTS
NOM. CONC. (g/l)
0
0.5
1
1.5
2
2.5
3
3.5
4
4.5
5
0.2
0.4
0.6
0.8

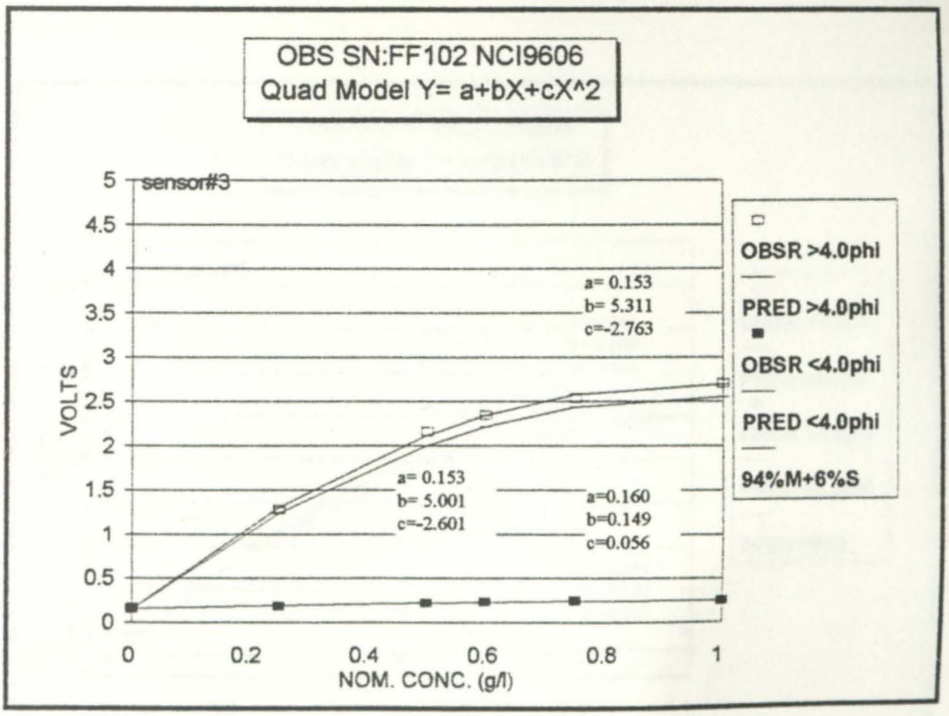
OBS SN:FF102 NCI9606
Quad Model Y= a+bX+cX^2
sensor#3
VOLTS
NOM. CONC. (g/l)
a= 0.153
b= 5.311
c=-2.763
a= 0.153
b= 5.001
c=-2.601
a=0.160
b=0.149
c=0.056
OBSR >4.0phi
PRED >4.0phi
OBSR <4.0phi
PRED <4.0phi
94%M+6%S

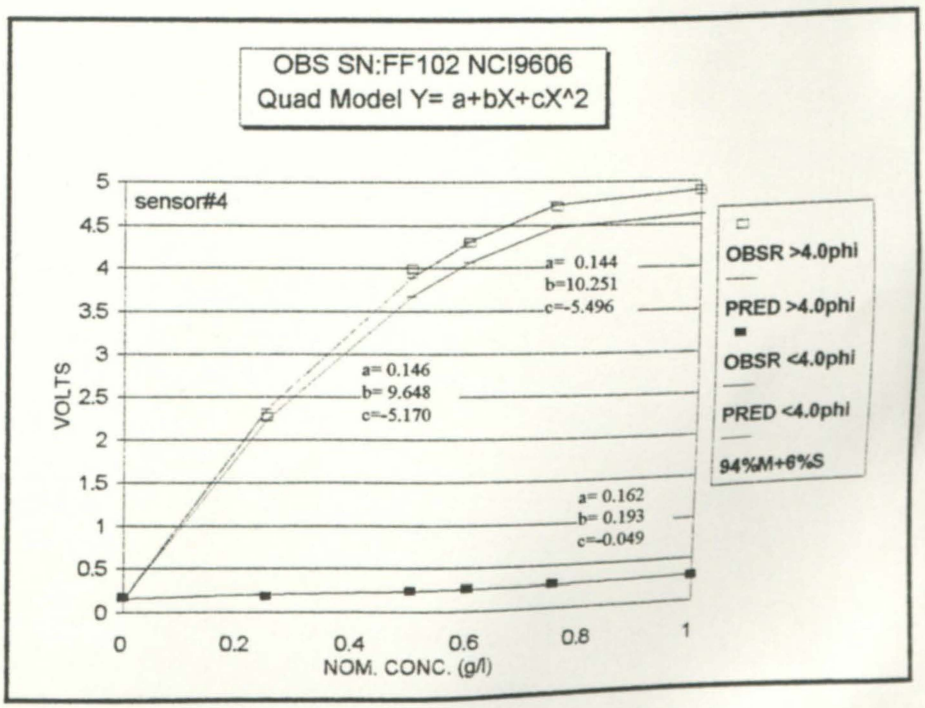
OBS SN:FF102 NCI9606
Quad Model Y= a+bX+cX^2
sensor#4
VOLTS
NOM. CONC. (g/l)
a= 0.144
b=10.251
c=-5.496
a= 0.146
b= 9.648
c=-5.170
a= 0.162
b= 0.193
c=-0.049
OBSR >4.0phi
PRED >4.0phi
OBSR <4.0phi
PRED <4.0phi
94%M+6%S

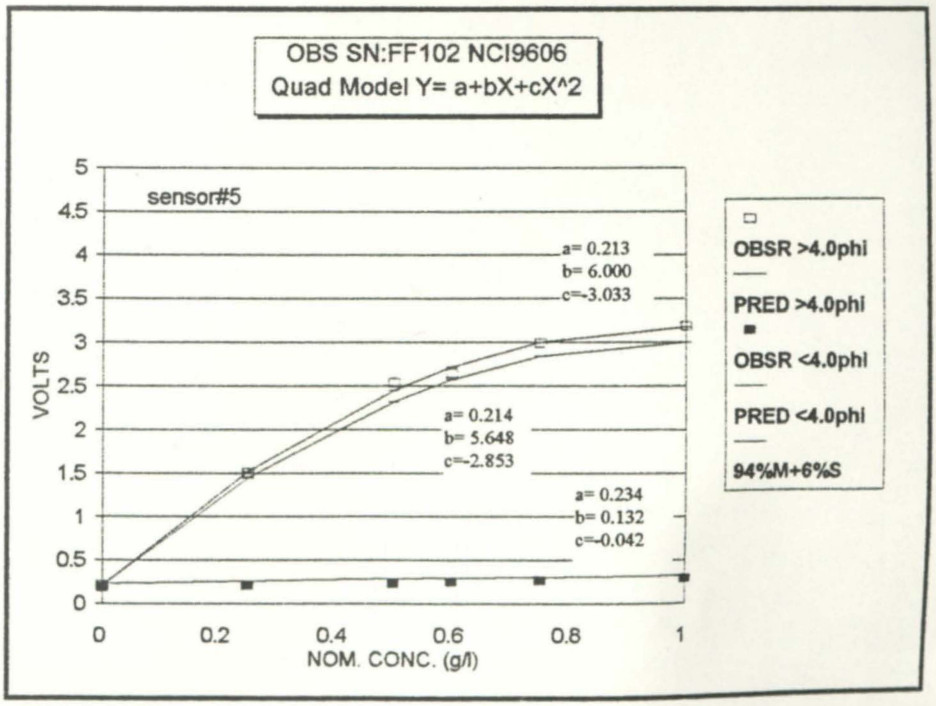
OBS SN:FF102 NCI9606
Quad Model Y= a+bX+cX^2
sensor#5
a= 0.213
b= 6.000
c=-3.033
a= 0.214
b= 5.648
c=-2.853
a= 0.234
b= 0.132
c=-0.042
VOLTS
NOM. CONC. (g/l)
OBSR >4.0phi
PRED >4.0phi
OBSR <4.0phi
PRED <4.0phi
94%M+6%S